

DynoSAM: Open-Source Smoothing and Mapping Framework for Dynamic SLAM

Jesse Morris*, Yiduo Wang, Mikolaj Kliniewski and Viorela Ila

Abstract—Traditional Visual Simultaneous Localization and Mapping (vSLAM) systems focus solely on static scene structures, overlooking dynamic elements in the environment. Although effective for accurate visual odometry in complex scenarios, these methods discard crucial information about moving objects. By incorporating this information into a Dynamic SLAM framework, the motion of dynamic entities can be estimated, enhancing navigation whilst ensuring accurate localization. However, the fundamental formulation of Dynamic SLAM remains an open challenge, with no consensus on the optimal approach for accurate motion estimation within a SLAM pipeline.

Therefore, we developed *DynoSAM*, an open-source framework for Dynamic SLAM that enables the efficient implementation, testing, and comparison of various Dynamic SLAM optimization formulations. *DynoSAM* integrates static and dynamic measurements into a unified optimization problem solved using factor graphs, simultaneously estimating camera poses, static scene, object motion or poses, and object structures. We evaluate *DynoSAM* across diverse simulated and real-world datasets, achieving state-of-the-art motion estimation in indoor and outdoor environments, with substantial improvements over existing systems. Additionally, we demonstrate *DynoSAM*’s utility in downstream applications, including 3D reconstruction of dynamic scenes and trajectory prediction, thereby showcasing potential for advancing dynamic object-aware SLAM systems. *DynoSAM* is open-sourced at <https://github.com/ACFR-RPG/DynoSAM>.

Keywords—SLAM, Mapping, RGB-D Perception, Dynamic SLAM

I. INTRODUCTION

Simultaneous Localization and Mapping (SLAM) has been a key area of research for over three decades [1]. Despite significant advancements, most SLAM systems are designed with the assumption of a predominantly static environment [2], [3], [4]. This limitation presents challenges in real-world scenarios, where dynamic objects are common and must be accounted for.

Traditionally, SLAM systems classify sensor measurements associated with moving objects as outliers, excluding such data from the estimation process [5], [6], and in doing so, discard valuable information about dynamic elements. Incorporating these objects into the SLAM framework enables accurate modeling of dynamic environments [7], [8], which directly benefits navigation and task planning systems [9], [10] and enhances the overall robustness of SLAM [11], [12].

Although learning-based methods have advanced robotic capabilities in dynamic environments, especially in autonomous

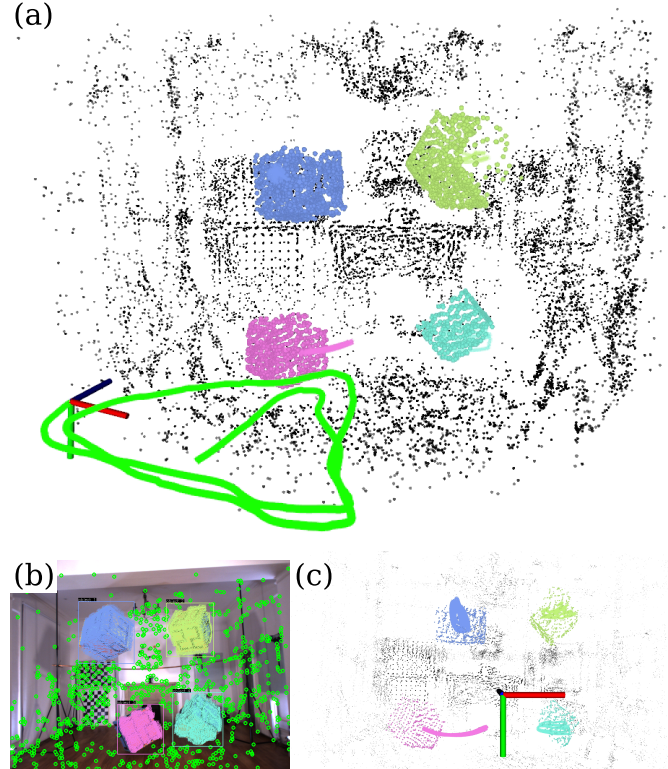


Fig. 1: *DynoSAM* is an open-source smoothing and mapping framework for Dynamic SLAM. The output of the system is shown in (a), which includes camera and object trajectories as well as the static and per-object dynamic map. (b) visualizes the feature-based front-end which performs multi-object tracking in addition to visual odometry. (c) shows dynamic map from the camera’s perspective, highlighting the estimated trajectory of each object and the tracked 3D points.

vehicle applications with access to large datasets, there remains a critical need for SLAM solutions in scenarios where motion models are unknown and data is scarce. These challenges are particularly pronounced when operating in unstructured environments [13] or space exploration applications [14].

As a result, there is increasing interest in extending SLAM systems to incorporate observations of dynamic entities and estimate their motions [1], [15], [16], [17], [18], [19]. In this paper we refer to such systems as *Dynamic SLAM*.

Recent advances in Dynamic SLAM have explored methods such as multi-object visual odometry techniques [17], [20] and graph-based optimization approaches [6], [15], [21]. The latter methods aim to jointly estimate for the robot pose, static structure, and the motion or trajectory of rigid-body objects in the scene using both static and dynamic point observations. The literature presents diverse approaches to formulating the Dynamic SLAM problem, each characterized by a distinct

* Corresponding author

Jesse Morris, Yiduo Wang, Mikolaj Kliniewski and Viorela Ila are with the Australian Centre For Robotics (ACFR), School of Aerospace, Mechanical and Mechatronic Engineering (AMME), University of Sydney, 2006 Sydney, Australia. {jesse.morris, yiduo.wang, mikolaj.kliniewski, viorela.ila}@sydney.edu.au

set of variables and objective functions, leading to different underlying graph structures. A recent study [18] compared object-centric approaches, where dynamic points or motions are represented in an object’s body frame, with world-centric approaches, where points and motions are modeled in the world frame. The findings demonstrated that the choice of variables and formulation has a substantial impact on the robustness, accuracy, and efficiency of SLAM systems.

Despite the growing interest in Dynamic SLAM research, there remains limited consensus on the best formulation to achieve accurate motion estimation. This motivated us to develop *DynoSAM*, a framework that provides a structured approach for implementing and evaluating Dynamic SLAM solutions. The proposed framework implements, evaluates and compares both existing approaches and new formulations for object motion and pose estimation, including those based on a world-centric [11], [15], [18] paradigm.

To rigorously evaluate these formulations, we have integrated them into a full Dynamic SLAM system that uses visual (stereo/RGB-D) sensor data as input, where Fig. 1 presents an example of our system estimating complex dynamic object motions in the Oxford Multimotion Dataset (OMD) [22]. Our framework uniquely models the motion of each object as a rigid-body pose change [23], offering flexibility in the parametrization of our estimation problem. We assess the accuracy and performance of our system using a variety of indoor and outdoor datasets.

DynoSAM is compared against other Dynamic SLAM pipelines [17], [15], [24], [21], where we achieve state-of-the-art accuracy in object motion and pose estimation. Furthermore, we demonstrate how our framework can be used to better inform downstream navigation applications by integrating *DynoSAM* with dynamic object reconstruction [8] and trajectory prediction methods.

II. CONTRIBUTIONS

The specific contributions of this paper are as follows:

- A framework for Dynamic SLAM that provides a structured approach for implementing, testing and evaluating graph-based solutions. Our framework establishes common terminologies and metrics for evaluating Dynamic SLAM pipelines, facilitating more robust conclusions and analysis. Within our framework we present a customizable recipe of formulations that serve as the theoretical foundation for a practical Dynamic SLAM system. We present a discussion and analysis for each method.
- A complete Dynamic Visual SLAM pipeline that incorporates all presented formulations in this paper. We evaluate the accuracy of our system on a variety of datasets.
- A novel formulation for Dynamic SLAM that directly parametrizes the pose of each object in the scene, whilst ensuring rigid-body kinematics are maintained.
- An exhaustive evaluation of our framework and proposed methodologies across various datasets, demonstrating state-of-the-art performance. To the best of our knowledge, this paper provides one of the most extensive evaluations of Dynamic SLAM formulations in the existing literature.

- An implementation of a sliding-window optimization approach to bound the computation. We analyze the impact on overall accuracy of the sliding-window compared to a full-batch approach.
- Integration of our Dynamic SLAM pipeline with downstream tasks highly relevant for navigation, such as dynamic object reconstruction [8] and trajectory prediction.

As part of our contribution we open-source our C++ implementation of *DynoSAM*, which is integrated with the Robotic Operating System 2 (ROS2) [25] and can be run with offline datasets or online data. Additionally, we provide data logging and serialization tools for each module to facilitate evaluation and debugging as well as an accompanying automated evaluation suite that has been used to generate all results in this paper. To facilitate modularity and parallelization of key components, *DynoSAM*’s architecture is inspired by Kimera [26].

III. RELATED WORK

This section provides an overview on how SLAM systems have been addressing the challenges of dynamic environments over the years. We discuss SLAM systems that aim to improve their robustness by removing or ignoring dynamic objects, as well as state-of-the-art Dynamic SLAM systems that estimates object poses and motions.

In order to handle the dynamic entities in the environment, conventional SLAM systems such as ORB-SLAM 3 [4] and DynaVINS [27] detect any moving observations as outliers and reject them to create a global map that only contains static structures using methods such as RANSAC [28], point correlations [29] and robust bundle adjustment formulation [27], [30]. Deep learning methods have also been recently used to semantically understand the scene, and detect and remove dynamic objects [6], [31], [32]. By taking an active approach in removing dynamic objects, these methods provide robust and accurate camera pose estimation in dynamic environments. However, any relevant information about the motion of the objects is discarded. Khronos [33] proposes a spatio-temporal SLAM formulation that attempts to unify short-term changes (such as dynamic objects) with long-term scene changes. They extract moving objects from their representation using a geometric motion detection method [34] and are able to construct a comprehensive map in complex, changing environments. However, they do not utilize any estimate of object motion and rely on a dense reconstruction pipeline to detect and track objects in the scene.

To represent the kinematic information of these objects, Dynamic SLAM methods incorporate measurements of dynamic entities in the SLAM formulation in addition to the static ones. These systems first segment dynamic observations from the static background using information such as kinematics [24], [17] and semantics [15], [21], [35], before optimizing the pose or motion of these objects jointly with the camera/robot poses and the map of the environment. Barsan *et al.* [36] leveraged semantic and kinematic segmentation to detect dynamic objects, tracked their motions using sparse scene flow and map them separately from the static scene, but they only handled frame-to-frame estimation without any joint optimization [36].

Within the Dynamic SLAM formulations that explicitly represent the object, the most common and intuitive approach is to directly estimate the object’s pose [21], [35], [37], [38]. Assuming each object is a rigid body, observed points on these objects are static in a body-fixed local object reference frame. By defining the poses of objects and in turn their local reference frames, there is an immediate advantage that each object point can be expressed in the object reference frame with a single variable in the optimization problem, reducing the overall number of variables in the system. Huang *et al.* [24], [35] cluster point observations on moving objects in a scene based on temporal rigidity to identify underlying rigid bodies. The resulting clusters of points defines the pose of each object and the poses of the camera and each dynamic object is solved through a sliding-window optimization. Their method, although able to extract dynamic objects from the scene, demonstrates poor object motion accuracy. Alternatively, several methods model objects using simple geometric primitives such as cuboids [39], [40], [41], [42] and ellipsoids [43] so as to define their poses. Recently, DynaQuadric [19] has proposed a joint optimization framework that reconstructs dynamic objects as quadrics. This unique representation allows the per-object scale to be explicitly defined and they demonstrate highly accurate camera localization. However, they evaluate only their object pose errors against other quadric-based methods and neglect object motion evaluations.

Several neural network-based methods have also been proposed in recent years [44], [45], [46], [47] to estimate the scene flow of 3D points or voxels. These systems focus on estimating the motions of individual points in the form scene flow vectors. While they produce impressive results, these systems do not recover the motions or poses of dynamic objects, and are therefore not further discussed in this paper.

When focusing on specific object types, BodySLAM++ [48] and DSP-SLAM [49] leverage learned object shape prior models in their formulation and achieve accurate object pose estimation. While their results demonstrate the benefit of integrating learned priors into a graph-based optimization framework, BodySLAM++ is restricted to only estimating human poses and DSP-SLAM provides no understanding on object dynamics. TwistSLAM [41] utilizes mechanical joint constraints to restrict the degrees of freedom for object motion estimation. While they demonstrate accurate pose estimation under constrained motion, their results suggest limitations in estimating the full SE(3) motion of objects, especially for objects with more complex motion patterns.

By comparison, other methods seek to estimate the full SE(3) motion of each object without the addition of semantic-specific constraints. Among these solutions, DynaSLAM II [21] takes an object-centric approach to motion estimation and reports the most accurate egomotion when compared with other approaches. By comparison, their experimental results demonstrate poor object motion estimation and the authors consider their use of sparse features to be the main reason behind such performance. However, our previous work [18] shows that the formulation used by [21] does not explicitly model the rigid-body kinematics, resulting in poor estimation accuracy even with a dense object representation.

An alternative formulation is to estimate object motions directly in a known reference frame, such as a camera frame that moves with a sliding window [17], [20], [22], or a well-defined reference frame like the world frame [18], [15], [50], which commonly coincides with the first camera/robot pose. MVO [17] represents the dynamic points in the camera frame, but models object motions in the object frame. They define object poses using point observations when each object is first observed, similar to the method of Bescos *et al.* [21].

Chirikjian *et al.* [23] demonstrated that a SE(3) motion can be expressed in any reference frame, and based this concept, VDO-SLAM [15], [11], [51] proposes a factor graph formulation to represent and estimate rigid-body object motions in the world frame without the need to estimate object poses. AirDOS [50] employs the same rigid-body motion model and extends it to articulated objects, e.g. humans, by combining it with a learning-based human pose estimator [52] to estimate for the motion of each segment of an articulated object. Interestingly, they quantitatively demonstrate direct improvement in their camera pose estimation due to the incorporation of dynamic objects. While the study of non-rigid body motion outside the scope of this paper, we find such a strategy inspiring for our future works. Our previous work [18] investigated the motion model employed by [15], [50] by comparing world and object-centric formulations and demonstrated that the world-centric approach better encodes rigid-body kinematic models, leading to more accurate motion estimation. Additionally, the world-centric approach exhibits more efficient convergence behavior and often requires shorter computation time despite requiring more variables. Development of [18] also highlighted practical challenges due to the limited availability of open-source Dynamic SLAM tools and systems which hindered rigorous comparison and evaluation. These limitations motivated the development of DynoSAM as a flexible and comprehensive framework for Dynamic SLAM.

IV. BACKGROUND

A. Rigid-Body Motion

Understanding rigid-body motion is fundamental to Dynamic SLAM because it provides a mathematical framework to model the motion of objects in the environment. Our framework utilizes this understanding to estimate the SE(3) motion of objects directly using frame-to-frame observations of 3D points on rigid bodies.

A motion is defined as any *change in pose*, following [23], which describes the conversion of one pose into another. Both poses and motions are represented using SE(3) homogeneous transformations. However, while a pose defines a body’s position and orientation relative to a reference frame, a motion maps one pose onto another. Our work leverages this concept and employs the three-index notation [23] for homogeneous transformations, allowing both the frame of reference and the frame in motion to be specified. For example, ${}^O_A \mathbf{H}_B \in \text{SE}(3)$ is the transformation which describes the motion from frame $\{A\}$ to frame $\{B\}$ from the perspective of frame $\{O\}$.

A rigid body, by definition, maintains its shape and size throughout motion and therefore, any rigid-body motion must

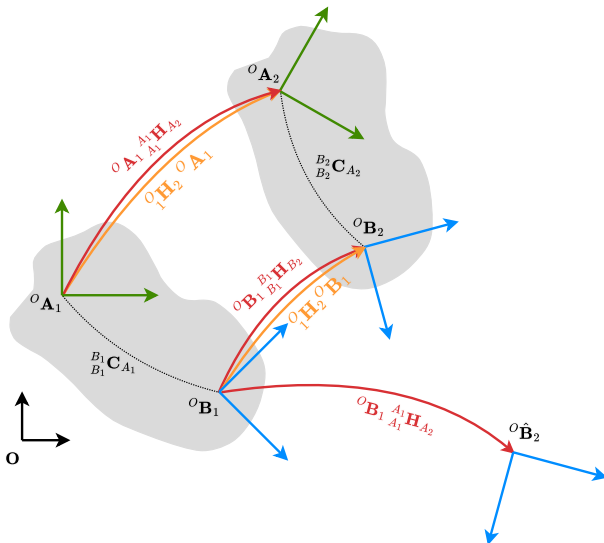


Fig. 2: Illustrative example showing the application of local (red) and observed (orange) motions on a rigid-body. Two arbitrary frames A and B are shown before and after a motion is applied to body. This figure illustrates that both local and observed motions can be used to correctly propagate the fixed frames ($\{A_1\}$ to $\{A_2\}$ and $\{B_1\}$ to $\{B_2\}$) in accordance with rigid-body kinematics. However, local motion is dependent upon the position and orientation of the reference frame, leading to the invalid propagation of $\{B_1\}$ to ${}^0\hat{B}_2$ if incorrectly applied.

ensure that the distance between any two points on the object remains constant. The work of [23] shows that while we can represent this rigid-body motion in any arbitrary frame, the observed motion of each point on the rigid-body depends on the frame of the observer. For instance, a point on a rotating wheel might appear stationary to an observer positioned locally on the same wheel but will appear to be moving rapidly to a stationary observer that is external to the wheel. Furthermore, we can also envisage an observer moving relative to the spinning wheel! This example illustrates the difference between *local* motion, which describes the motion as perceived by (or on) the object, and *observed* motion, which describes the motion as perceived by an external observer.

Since it is our goal to estimate the object's rigid-body motion from observing a small set of individual points, consider attempting to estimate the rigid-bodies local motion: each point observed will exhibit their own unique local motion, thus making it complex to directly infer the overall motion of the rigid-body. This challenge can be overcome by instead considering the motion of each point on the rigid body as observed by an external reference frame. *By representing points on the rigid-body in a common, external reference frame, the motion of all points, and hence, the body itself, can be described using a single SE(3) transformation.* This approach is highly relevant in Dynamic SLAM as only partial observations of an object are often possible and the observed motion representation allows all point observations to directly contribute to estimating the object's overall motion.

To further illustrate these concepts, consider the two arbitrary reference frames $\{A_1\}$ and $\{B_1\}$ as depicted in Fig. 2. Both frames are rigidly attached to the shown rigid body. After some motion is applied to the body, their corresponding

frames are shown as $\{A_2\}$ and $\{B_2\}$. All frames are defined with their associated poses ${}^0\mathbf{A}_1$, ${}^0\mathbf{B}_1$, ${}^0\mathbf{A}_2$ and ${}^0\mathbf{B}_2$ with respect to the fixed origin frame $\{O\}$. Vitally, since the body is rigid, the relative pose transformation between frames A and B remains constant over time and defines the kinematic constraints of a rigid body. We denote these pose transformations as ${}^{B_1}\mathbf{C}_{A_1} = \mathbf{C} = {}^{B_2}\mathbf{C}_{A_2}$. Contrastingly, we use \mathbf{H} to specify any motion described by a homogeneous transformation.

1) *Local Motion:* Local motion describes the process of moving a coordinate frame from one pose relative to another and can be thought of as the motion of the frame as *perceived by the object*. A transformation of this form can be clearly specified using the three-indexed notation ${}^A\mathbf{H}_B$. As noted in [23], the robotics community commonly uses this representation by default, allowing for the simpler notation such as ${}^A\mathbf{H}_B$.

We use Fig. 2 to illustrate how local motion (shown on the figure in red) can be used to correctly propagate frames $\{A_1\}$ to $\{A_2\}$ and $\{B_1\}$ to $\{B_2\}$:

$$\begin{aligned} {}^0\mathbf{A}_2 &= {}^0\mathbf{A}_1 {}^{A_1}\mathbf{H}_{A_2} \\ {}^0\mathbf{B}_2 &= {}^0\mathbf{B}_1 {}^{B_1}\mathbf{H}_{B_2}. \end{aligned} \quad (1)$$

In this context 'correctly' means that no rigid-body kinematic constraint are violated. However, the applicability of local motion is constrained by the position and orientation of the reference frame, making it dependent on the frame's origin. Such limitation can lead to inconsistencies when propagating frames with different origins; this specific case is illustrated in Fig. 2 where ${}^{A_1}\mathbf{H}_{A_2}$ is used to propagate frame $\{B_1\}$. The resulting pose ${}^0\mathbf{B}_2$ clearly violates rigid-body constraints.

2) *Observed Motion:* Observed motion describes the motion of a rigid-body as seen by an external observer. Fig. 2 uses orange arrows to depict the propagation $\{A_1\}$ and $\{B_1\}$ using the observed motion ${}^0\mathbf{H}_2$, which is defined with respect to the origin frame $\{O\}$. In contrast to local motion in Eq. (1), the same observed motion ${}^0\mathbf{H}_2$ can propagate both $\{A_1\}$ and $\{B_1\}$ in accordance with rigid-body kinematics. This is possible because the observed motion representation is independent of the position and orientation of the frame that it is acting upon.

While these underlying principles have been previously established, notably in [23] and subsequently applied to the estimation problems in our prior works [11], [15], [18], a full derivation of observed motion within the context of Dynamic SLAM has not been previously presented. We believe a more complete derivation is crucial for understanding the benefits of this representation. In this section, we exploit the constraints of a rigid body to show how ${}^0\mathbf{H}_2$ can be derived given the relations defined in Eq. (1) and the constant relative transformation \mathbf{C} between $\{A\}$ and $\{B\}$. By applying a frame change of a pose transformation [23] we can express each local motion in a common origin frame:

$$\begin{aligned} {}^0\mathbf{H}_2 &:= {}^0\mathbf{A}_1 {}^{A_1}\mathbf{H}_{A_2} {}^0\mathbf{A}_1^{-1} \\ &= {}^0\mathbf{B}_1 {}^{B_1}\mathbf{C}_{A_1} {}^{A_1}\mathbf{H}_{A_2} {}^{B_1}\mathbf{C}_{A_1}^{-1} {}^0\mathbf{A}_1^{-1} \\ &= {}^0\mathbf{B}_1 {}^{B_1}\mathbf{C}_{A_1} {}^{A_1}\mathbf{H}_{A_2} {}^{B_2}\mathbf{C}_{A_2}^{-1} {}^0\mathbf{A}_1^{-1} \\ &= {}^0\mathbf{B}_1 {}^{B_1}\mathbf{H}_{B_2} {}^0\mathbf{B}_1^{-1}. \end{aligned} \quad (2)$$

Eq. (2) shows that ${}^O\mathbf{H}_2$ remains constant regardless of the choice of \mathbf{A} and \mathbf{B} and, therefore, this representation of motion is independent of the rigid body's frame of reference. Furthermore, using Eq. (1), we can rewrite Eq. (2) as:

$${}^O\mathbf{H}_2 = {}^O\mathbf{A}_2 {}^O\mathbf{A}_1^{-1} = {}^O\mathbf{B}_2 {}^O\mathbf{B}_1^{-1}, \quad (3)$$

allowing new composition relationships to be established:

$$\begin{aligned} {}^O\mathbf{A}_2 &= {}^O\mathbf{H}_2 {}^O\mathbf{A}_1 \\ {}^O\mathbf{B}_2 &= {}^O\mathbf{H}_2 {}^O\mathbf{B}_1. \end{aligned} \quad (4)$$

We highlight that the composition order of the observed motion in Eq. (4) is not the same as that for the local motion in Eq. (1) due to their fundamental differences, and we direct the interested reader to [23] for more details.

B. Notations

We define the notations for the Dynamic SLAM problem by considering a scene at a discrete time-step k with a set of objects and their associated poses with respect to a fixed world frame $\{W\}$ denoted as ${}^W\mathcal{L}_k$:

$${}^W\mathcal{L}_k = \{{}^W\mathbf{L}_k^j \in \text{SE}(3), j \in \mathcal{J}_k, k \in \mathcal{K}\}$$

where \mathcal{J}_k is the set of object indices observed at time-step k and \mathcal{K} contains all time-steps of the sequence. Each object pose ${}^W\mathbf{L}_k^j$ is associated with a body-fixed reference frame $\{L_k\}$. For the j -th object, we define its observation history ${}^W\mathcal{L}$ using the $n+1$ consecutive frames that the object has been observed in ${}^W\mathcal{L}^j = \{{}^W\mathbf{L}_k^j\}_{k=s \dots s+n}$, where s is the first time-step at which this object is observed. Using this notation we can write the first pose of the object trajectory as ${}^W\mathbf{L}_s^j$. Similarly, ${}^W\mathbf{X}_k \in \text{SE}(3)$ is the camera pose with respect to the world frame $\{W\}$ at time-step k , and is associated with a camera frame $\{X_k\}$. The set of all camera poses is denoted as ${}^W\mathcal{X} = \{{}^W\mathbf{X}_k \in \text{SE}(3), k \in \mathcal{K}\}$

We denote $\mathbf{m}^i = [\tilde{\mathbf{m}}^i, 1]^\top$ as the homogeneous coordinates of a 3D point $\tilde{\mathbf{m}}^i \in \mathbb{R}^3$, where i is a unique tracklet index and indicates correspondences across frames. Any point in the world frame can be transformed into the camera frame:

$${}^{X_k}\mathbf{m}_k^i = {}^W\mathbf{X}_k^{-1} {}^W\mathbf{m}_k^i.$$

We use \mathbf{m} to refer to both static and dynamic points. In the case of a static point, ${}^W\mathbf{m}_k \doteq {}^W\mathbf{m}$ as we omit the time-step k to indicate the variable is time invariant. Finally, ${}^W\mathcal{M}_k$ refers to the set of all points in the world frame at k .

We denote motion of the camera as \mathbf{T} and the motion of any object j as \mathbf{H} . From now onwards we use \mathbf{H} to only refer to the motion of objects, rather denoting general motion as in Sec. IV-A. Between time-steps $k-1$ and k the local motions of the camera and object are ${}^{X_{k-1}}\mathbf{T}_{X_k}$ and ${}^{L_{k-1}}\mathbf{H}_{L_k}$ respectively. In the case where our notation is already explicit in denoting which pose the transformation is referring to, i.e., camera pose with \mathbf{T} or object pose with \mathbf{H} , we simplify the notation by only using time-steps:

$$\begin{aligned} {}^{X_{k-1}}\mathbf{T}_k &\doteq {}^{X_{k-1}}\mathbf{T}_{X_k} \\ {}^{L_{k-1}}\mathbf{H}_k &\doteq {}^{L_{k-1}}\mathbf{H}_{L_k} \end{aligned} \quad (5)$$

These transformations describe local motions and, following Eq. (1), can be used to propagate the camera and object poses from $k-1$ to k :

$${}^W\mathbf{X}_k = {}^W\mathbf{X}_{k-1} {}^{X_{k-1}}\mathbf{T}_k \quad (6)$$

$${}^W\mathbf{L}_k = {}^W\mathbf{L}_{k-1} {}^{L_{k-1}}\mathbf{H}_k \quad (7)$$

For the purposes of object motion estimation, our framework uses an observed motion representation, as discussed in Sec. IV-A2. In the context of SLAM this reference frame can be any observable frame, e.g. the camera frame at the start of a sliding-window. In this work, we represent our object motions in the world frame $\{W\}$, as introduced by our previous works [11], [15], [18]. Such a representation is convenient for downstream applications like mapping and planning, as it allows all state variables in our formulations to be defined with respect to a common coordinate system. For any object j this motion is denoted as ${}_{k-1}^W\mathbf{H}_k$. Due to its representation in the the world frame we refer specifically to it as the *absolute* motion.

Using Eq. (3) we define our absolute motion in terms of a change in object pose:

$${}_{k-1}^W\mathbf{H}_k = {}^W\mathbf{L}_k {}^W\mathbf{L}_{k-1}^{-1} \quad (8)$$

Following the composition rules defined in Eq. (4), ${}_{k-1}^W\mathbf{H}_k$ will move ${}^W\mathbf{L}_{k-1}$ to ${}^W\mathbf{L}_k$ when applied on the left-hand side:

$${}^W\mathbf{L}_k = {}_{k-1}^W\mathbf{H}_k {}^W\mathbf{L}_{k-1}. \quad (9)$$

Vitally, this propagation also holds for any point i on a rigid-body:

$${}^W\mathbf{m}_k^i = {}_{k-1}^W\mathbf{H}_k {}^W\mathbf{m}_{k-1}^i, \quad (10)$$

relating the motion of *any and all* points on an object with a single transformation. Since we can directly observe 3D object points, Eq. (10) allows us to easily derive cost functions in terms of all tracked points on the object. This equation underpins all our formulations and is fundamental to our Dynamic SLAM framework. A more detailed derivation of Eq. (10) is included in Appendix A which highlights how this equation implicitly encodes the rigid-body kinematic constraints discussed in Sec. IV-A.

As before, we define the set of object motions at timestamp k for all objects $j \in \mathcal{J}_k$ as:

$${}_{k-1}^W\mathcal{H}_k = \{{}_{k-1}^W\mathbf{H}_k^j, j \in \mathcal{J}_k, k \in \mathcal{K}\}$$

For all notation we often omit indices i and j when there is no ambiguity.

V. FOUNDATIONS FOR DYNAMIC SLAM

This section details the graph-based Dynamic SLAM formulations included within our framework. We demonstrate how the concept of observed motion, explained in Sec. IV, is applied to directly estimate both object motions (Sec. V-B) and poses (Sec. V-C). These formulations constitute the back-end of a visual Dynamic SLAM pipeline. As a result, we assume dynamic objects can be tracked and 3D point measurements of static and dynamic features can be provided by a visual SLAM front-end. While we outline our front-end (Sec. VI-B) and

include it in our open-source implementation, the formulations discussed in our framework are agnostic to any particular front-end designs.

For each approach, we define residual functions \mathbf{r} associated with covariance matrices Σ . These are used to construct factors ϕ in the form:

$$\phi(\cdot) \propto \exp\left\{-\frac{1}{2}\|\mathbf{r}\|_{\Sigma}^2\right\} \quad (11)$$

Under the standard assumption of zero-mean Gaussian noise, we take the negative log of Eq. (11) and drop the scaling-factor allowing us to collect all residuals and construct a nonlinear least-squares problem:

$$\mathbf{r}^{\text{MAP}} = \underset{\mathcal{X}}{\text{argmin}} \sum \|\mathbf{r}\|_{\Sigma}^2 \quad (12)$$

For completeness, our framework also includes the object-centric formulations explored in [18]. However, due to their inferior performance, this work does not discuss them further.

A. Measurements

We define the following notation for visual features. Direct measurements are denoted as $\mathbf{z}_{2D} \in \mathbb{R}^2$ and represent 2D pixel measurements on the image plane. We denote 3D point measurements in the local sensor frame $\{X\}$ as $\mathbf{z}_{3D} \in \mathbb{R}^3$. In the context of stereo/RGB-D SLAM, we assume the depth d of each pixel measurement \mathbf{z}_{2D} is available for every time-step k , and 3D measurements are constructed accordingly:

$$[\mathbf{z}_{3D}, 1]^T = {}^{X_k} \mathbf{m}_k = \pi^{-1}(\mathbf{z}_{2D}, d). \quad (13)$$

where $\pi^{-1}(\cdot)$ is the sensors back-projection function, e.g. pinhole camera model. We further specify the notation for sets of measurements corresponding to static and dynamic entities. $\mathcal{S}_{2D,k}$ and $\mathcal{S}_{3D,k}$ denote the set of static 2D keypoints \mathbf{z}_{2D} and their corresponding 3D landmark measurements \mathbf{z}_{3D} at time k , respectively. Similarly, $\mathcal{D}_{2D,k}$ and $\mathcal{D}_{3D,k}$ are the sets of dynamic measurements. The set of all static measurements (2D and 3D) is denoted as \mathcal{S}_k . \mathcal{D}_k is the set of all dynamic measurements. The set of dynamic measurements on a particular object is specified using the super-script j , e.g. $\mathcal{D}_{3D,k}^j$ is the sub-set of 3D measurements on object j at time k .

B. World-Centric Motion Estimator

The world-centric motion formulation directly estimates for object motions and their rigid-structure, as well as the static scene and camera pose:

$$\theta \doteq [{}^W \mathbf{X}_k, {}_{k-1}^W \mathbf{H}_k, {}^W \mathcal{M}_k], k \in \mathcal{K}. \quad (14)$$

This formulation was first proposed in [15] and then rigorously evaluated in [18], establishing it as a highly accurate method for object motion estimation. Fig. 3 shows the corresponding factor graph for this formulation and includes three static landmarks (blue) and one landmark (orange) on a dynamic object that are tracked over three frames.

Given a 3D observation of a point (static or dynamic), we constrain the point to the world frame using a *point measurement factor*:

$$\mathbf{r}_{3D,R} = \mathbf{z}_{3D,k} - {}^W \mathbf{X}_k^{-1} {}^W \mathbf{m}_k. \quad (15)$$

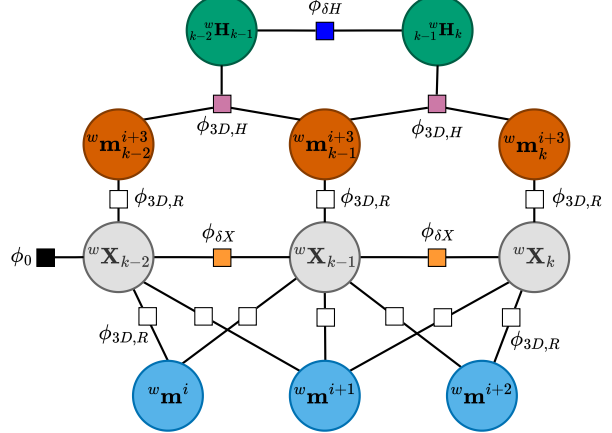


Fig. 3: World-centric motion formulation factor-graph. We show three static landmarks (blue) and one landmark on a dynamic object (orange), tracked over three frames. Camera poses are shown in grey and object motion in green. The *point measurement factor* ($\phi_{3D,R}$) is shown in white, the *ternary motion factor* ($\phi_{3D,H}$) in magenta and the *object motion smoothing factor* ($\phi_{\delta H}$) in dark blue. The prior factor on the first camera pose is shown in black.

For every static point, ${}^W \mathbf{m}$ is initialized as ${}^W \mathbf{m} = {}^W \mathbf{X}_k \mathbf{z}_{3D,k}$ when the point is first observed. We use the same method to initialize each dynamic point at every frame k .

The relative transformation between consecutive camera poses is modeled using the *between factor*:

$$\mathbf{r}_{\delta X} = \left[\log \left({}_{k-1}^{X_{k-1}} \mathbf{T}_k^{-1} {}^W \mathbf{X}_{k-1}^{-1} {}^W \mathbf{X}_k \right) \right]^{\vee}, \quad (16)$$

where the odometry ${}_{k-1}^{X_{k-1}} \mathbf{T}_k$ can be estimated by the front-end of a visual SLAM system, such as the proposed one described in Sec. VI-B, or from alternative sources such as an Inertial Measurement Unit (IMU) if available. The operation $[\log(\cdot)]^{\vee}$ maps an SE(3) transformation to \mathbb{R}^6 .

From Eq. (10) we derive the *ternary object motion factor* which models the motion of any point i on a rigid body j as in [15], [18]:

$$\mathbf{r}_{3D,H} = {}^W \mathbf{m}_k^i - {}_{k-1}^W \mathbf{H}_k {}^W \mathbf{m}_{k-1}^i, \quad (17)$$

This cost function relates a pair of tracked points on a rigid-body object with the object motion.

Finally, for each object j an *object smoothing factor* is introduced between consecutive motions:

$$\mathbf{r}_{\delta H} = \left[\log \left({}_{k-2}^W \mathbf{H}_{k-1}^{-1} {}_{k-1}^W \mathbf{H}_k \right) \right]^{\vee}. \quad (18)$$

This enforces a constant motion model represented in $\{W\}$ and prevents abrupt, drastic and unrealistic changes in object motions between consecutive frames. Previous work [11] shows that if the motion is constant in the body frame, then the reference frame pose change is also constant; an extended version of this proof is included in Appendix B.

The nonlinear least-squares problem is constructed using the

combination of these factors:

$$\begin{aligned} \theta^{\text{MAP}} = \underset{\theta}{\text{argmin}} & \left(\|\mathbf{r}_0\|_{\Sigma_0}^2 + \|\mathbf{r}_{\delta X}\|_{\Sigma_{\delta X}}^2 \right. \\ & + \sum_{m \in \mathcal{S}_{3D,k}} \rho_h \|\mathbf{r}_{3D,R}\|_{\Sigma_{3D,R}}^2 \\ & + \sum_{m \in \mathcal{D}_{3D,k}} \rho_h \|\mathbf{r}_{3D,R}\|_{\Sigma_{3D,R}}^2 \\ & + \sum_{j \in \mathcal{J}_k} \sum_{m \in \mathcal{D}_{3D,k}^j} \rho_h \|\mathbf{r}_{3D,H}\|_{\Sigma_{3D,H}}^2 \\ & \left. + \sum_{j \in \mathcal{J}_k} \|\mathbf{r}_{\delta H}\|_{\Sigma_{\delta H}}^2 \right), \end{aligned} \quad (19)$$

where \mathbf{r}_0 is prior residual on the first camera pose state variable and ρ_h is a robust cost function. In our implementation we use the Huber [53] function, although any robust cost can be used.

While not being directly incorporated in this estimation, the trajectory of each object ${}^W\mathcal{L}$ can be recovered by recursively propagating the previous pose using the estimated motion following Eq. (9). This method requires an arbitrary first pose ${}^W\mathbf{L}_s$ to be defined, which anchors the resulting trajectory. Since the estimated motion is an absolute motion, we can define this pose anywhere relative to $\{W\}$. Practically, we construct ${}^W\mathbf{L}_s$ upon the initial observation of an object using the centroid of all object point observations as its position and identity as its orientation. However, any method that provides object pose, such as learned techniques can easily be adopted. For evaluation, we use the ground truth object pose to set ${}^W\mathbf{L}_s$. This ensures that the estimated object trajectories and the ground truth have aligned origins which facilitates proper evaluation as discussed in Sec. VII-A.

C. World-Centric Pose Estimator

While estimating ${}_{k-1}^W\mathbf{H}_k$ provides valuable information about object dynamics, directly estimating object pose ${}^W\mathbf{L}_k$ can offer a more comprehensive understanding of the scene. As seen in the literature, object pose enables more direct reasoning about the semantic and geometric properties of objects, facilitating tasks such as scene understanding and object-centric planning. We therefore further propose a novel approach that directly estimates for the object pose:

$$\theta \doteq [{}^W\mathbf{X}_k, {}^W\mathcal{L}_k, {}^W\mathcal{M}_k] \quad k \in \mathcal{K} \quad (20)$$

The core of this approach is as follows: Eq. (8) shows how a motion ${}_{k-1}^W\mathbf{H}_k$ explicitly models a pair of consecutive object poses. Using this idea, we reformulate our factors to make every ${}^W\mathbf{L}$ a variable of the system. The corresponding factor graph is shown in Fig. 4. Substituting Eq. (8) into Eq. (17) forms a new *quaternary object motion factor*:

$$\mathbf{r}_{3D,LL} = {}^W\mathbf{m}_k^i - {}^W\mathbf{L}_k {}^W\mathbf{L}_{k-1}^{-1} {}^W\mathbf{m}_{k-1}^i. \quad (21)$$

We similarly define the smoothing factor in-terms of object pose by substituting Eq. (8) into Eq. (18). This forms the *object*

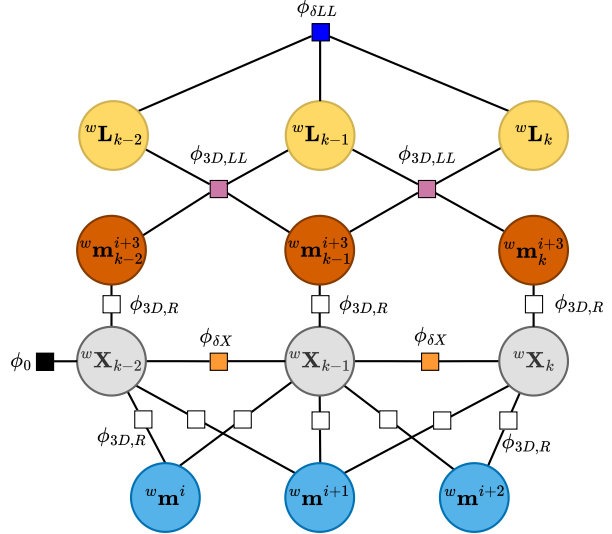


Fig. 4: World-centric pose formulation factor graph. As with the previous formulation (shown in Fig. 3), three static landmarks (blue) and one dynamic landmark (orange) are shown. The object pose, \mathbf{L} , is shown in yellow with the modified motion ($\phi_{3D,LL}$) and smoothing factor ($\phi_{\delta LL}$) in magenta and dark blue respectively.

pose smoothing factor:

$$\mathbf{r}_{\delta LL} = \left[\log \left(\left({}^W\mathbf{L}_{k-1} {}^W\mathbf{L}_{k-2}^{-1} \right)^{-1} \left({}^W\mathbf{L}_k {}^W\mathbf{L}_{k-1}^{-1} \right) \right) \right]^\vee \quad (22)$$

The nonlinear least-squared problem is constructed as:

$$\begin{aligned} \theta^{\text{MAP}} = \underset{\theta}{\text{argmin}} & \left(\|\mathbf{r}_0\|_{\Sigma_0}^2 + \|\mathbf{r}_{\delta X}\|_{\Sigma_{\delta X}}^2 \right. \\ & + \sum_{s \in \mathcal{S}_{3D,k}} \rho_h \|\mathbf{r}_{3D,R}\|_{\Sigma_{3D,R}}^2 \\ & + \sum_{d \in \mathcal{D}_{3D,k}} \rho_h \|\mathbf{r}_{3D,R}\|_{\Sigma_{3D,R}}^2 \\ & + \sum_{j \in \mathcal{J}_k} \sum_{m \in \mathcal{D}_{3D,k}^j} \rho_h \|\mathbf{r}_{3D,LL}\|_{\Sigma_{3D,LL}}^2 \\ & \left. + \sum_{j \in \mathcal{J}_k} \|\mathbf{r}_{\delta LL}\|_{\Sigma_{\delta LL}}^2 \right) \end{aligned} \quad (23)$$

Unlike other Dynamic SLAM methods which also estimate for object pose, our formulation continues to model dynamic points directly in the world frame rather than using an object-centric representation. This avoids the problems of object-centric formulations, as outlined in [18]. Furthermore, by simply re-parameterizing our cost functions in terms of pose we can ensure that our formulation directly embeds the observed motion model, which allows us to define $\{L\}$ anywhere on the object. This flexibility enables the integration of various initialization methods, such as SLAM front-ends or observation centroids, without compromising rigid-body kinematic constraints.

VI. SYSTEM

Based on the formulations discussed in Sec. V, we present the DynoSAM pipeline, a factor-graph based Dynamic Visual

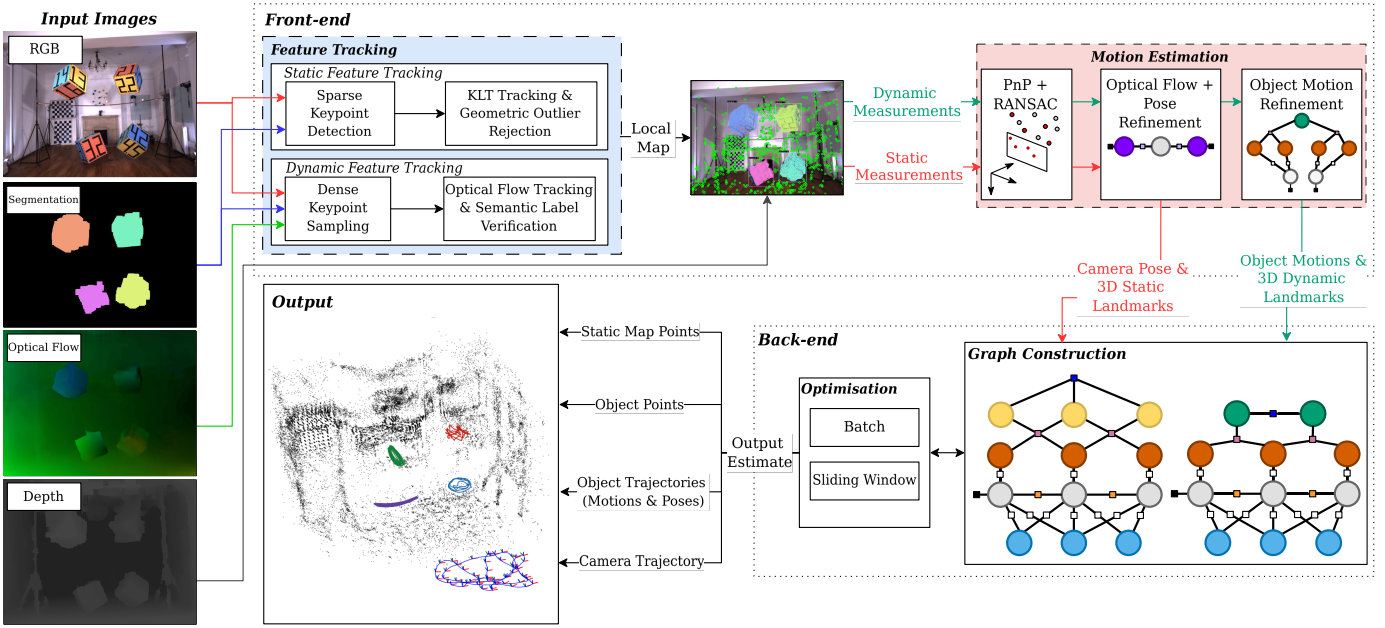


Fig. 5: DynoSAM system diagram. Our pipeline receives RGB, Segmentation, Optical Flow and Dense Depth images (on the left) as input and outputs static/dynamic map points, object and robot trajectories. A complete front-end is included for feature and object tracking as well as a back-end where different Dynamic SLAM formulations are implemented.

SLAM system. For input, our pipeline takes stereo/RGB-D, instance segmentation masks and dense optical flow, and produces globally consistent trajectories of the camera and objects as well as the static structure and temporal map of each object. The system diagram is shown in Fig. 5.

Our pipeline is broken into the typical front-end-backend structure. The front-end (Sec. VI-B) processes image data to generate static and dynamic feature tracks and provides initial estimates for the back-end. The front-end is responsible for object-level data association across frames, ensuring that features are consistently tracked on the same object to enable robust estimation. The back-end (Sec. VI-C) fuses static and dynamic measurements via a GTSAM-based [54] factor-graph optimization to produce a globally consistent estimate of the dynamic scene. Our implementation can perform full-batch smoothing where the system is optimized over all measurements, or a sliding-window estimation which bounds the size of the optimization problem.

We implement both the world-centric motion and pose formulations explained in Sec. V as part of our system, and exhaustively test and analyze them on a wide variety of datasets, the result of which is presented in Sec. VII.

A. Image Preprocessing

The front-end requires a set of four images \mathcal{I}_k as input per time-step. Each \mathcal{I}_k consists of a RGB image I_k^R , an instance segmentation I_k^S , per-pixel optical-flow I_k^F , and per-pixel depth I_k^D , as shown in Fig. 5. We undistort and align I_k^R with the depth image I_k^D that is obtained from an RGB-D or stereo camera system. Both depth and optical-flow are expected to be dense and can be obtained from classical [55] or learned methods [56]. Finally, I_k^S is used in the process of masking out dynamic objects from the static background. Our system requires all background pixels to be labeled as 0 and

object pixels in the scene are labeled $1 \dots n_o$. This processing is performed online as an integral part of our complete SLAM pipeline, using built-in algorithms to compute dense optical flow and semantic instance segmentation from I_k^R .

B. Front-end

The DynoSAM front-end performs per-frame visual tracking, producing an initial estimation of camera pose ${}^W\mathbf{X}_k$ and per-object motions ${}_{k-1}\mathcal{H}_k$ as well as a set of visual measurements as defined in Sec. V-A:

$$\mathcal{Z}_k = \{\mathcal{S}_k, \mathcal{D}_k\}.$$

The reminder of this section introduces each front-end module. The Feature Detection & Tracking module (Sec. VI-B1) generates \mathcal{Z}_k by tracking static and dynamic features from \mathcal{I}_k . These measurements support camera pose estimation (Sec. VI-B2) and multi-object motion estimation (Sec. VI-B3). Joint Optical-Flow (Sec. VI-B4) and Object Motion Refinement (Sec. VI-B5) components are used to further refine camera pose and object motion estimates.

1) *Feature Detection & Tracking*: The feature detection and tracking module matches corresponding static and per-object features between consecutive frames. I_k^R and I_k^F are used for feature detection and tracking while I_k^S is used to determine if a keypoint belongs to the static background or a dynamic object. The module ensures consistent tracking of features on the same object while maintaining sufficient spread and density of features across frames, thereby preserving the accuracy of both visual odometry and object motion estimation.

After detection and tracking, all features are initially marked as inliers and may be marked as outliers during the motion estimation module as visualized in Fig. 5. Once both static and dynamic keypoints are tracked, we use the input depth map I_k^D to directly obtain 3D measurements $\mathcal{D}_{3D,k}$ and $\mathcal{S}_{3D,k}$

from 2D pixel measurements, forming the local map shown in Fig. 5. We provide a detailed explanation below.

Static Feature Tracking. At each time-step, a *sparse* set of detected static keypoints $S_{2D,k}$ are tracked across consecutive frames using optical flow. Our framework offers options to select different feature extraction algorithms depending on the use case; for our experiments we used Shi-Tomasi corners [57] for indoor environments and ORB [58] features for outdoor environments. By default, our front-end uses the Lucas-Kanade tracker [59] to generate feature correspondences. The input optical flow I_k^F can also be used when it is reliable. Once tracked, our front-end performs geometric verification to discard poor correspondences.

To improve robust tracking, we retain only relevant features by applying Adaptive Non-Maximal Suppression (ANMS) [60] to the detected keypoints. This procedure retains only the most informative and reliable features, while simultaneously promoting a spatially uniform distribution of features across the image. ANMS achieves this by culling uninformative features whilst ensuring that a minimum number of features remain (800 in our experiments). Our front-end will detect new keypoints on the static structure if the number of inlier tracks falls below this minimum threshold. This adaptive mechanism ensures that a consistently high number of well-distributed features are tracked across successive frames, thereby enhancing tracking robustness and accuracy.

Dynamic Feature Tracking. For dynamic objects, we seek to track a *dense* set of features for each object, $\mathcal{D}_{2D,k}$. Dense tracking is important to achieve good coverage over the entire observable object for robust motion estimation [51]. For each dynamic measurement we maintain an associated object-level label j , such that features can be associated to the same object between frames.

The instance segmentation mask I_k^S is used to retrieve the object label j per pixel. While this mask can be generated from any standard instance segmentation network, many of these networks do not guarantee that the instance labels will be temporally consistent. Before tracking dynamic keypoints, object masks are tracked using [61]. We then remap the original instance labels to a temporally consistent label j per object. If the user has their own instance segmentation and tracking method, they can choose to bypass this algorithm. In that case, the user only needs to ensure that each pixel represents the unique tracking label j .

Although the instance segmentation mask I_k^S is able to separate objects from the background, it cannot distinguish between static and moving objects. To address this, we use the method from [51] to identify moving objects based on scene flow, allowing us to focus on tracking features only on the dynamic objects. This module can be easily modified to integrate learning-based approaches to identify moving objects in the scene.

Once the moving objects in the image are identified and tracked, dense features are extracted by sampling keypoints uniformly within each tracked object mask. The optical flow image I_k^F is then used directly to find the correspondences between frames. Our tracking algorithm ensures that, where possible, a consistent and significant number of

features (800 in our experiments) on each object are maintained and tracked. Similarly to static points, only inliers from the previous frame are used.

2) *Initial Camera Pose Estimation:* At each time-step, static measurements \mathcal{S}_k are used to estimate the initial camera pose. As shown in the motion estimation module in Fig. 5, the first step is the PnP algorithm [62] which estimates ${}^W\mathbf{X}_k$ by minimizing the re-projection error:

$$\mathbf{r}_{2D,R} = \mathbf{z}_{2D,k}^i - \pi({}^W\mathbf{X}_k^{-1} {}^W\mathbf{m}^i) \quad (24)$$

between the tracked static keypoints in the current frame at time-step k and the local map constructed from the previous frame. RANSAC verification and outlier rejection is performed using the implementation as provided by OpenGV [63] to obtain robust initial estimation of the camera pose. This initial camera pose is further refined through joint optical flow and pose optimization method detailed in Sec. VI-B4.

3) *Initial Object Motion Estimation:* The initial object motion ${}_{k-1}^W\mathbf{H}_k \in \mathcal{H}_k$ is estimated following the method of Zhang *et al.* [15]:

$$\mathbf{r} = \mathbf{z}_{2D,k}^i - \pi({}^W\mathbf{X}_k^{-1} {}_{k-1}^W\mathbf{H}_k {}^W\mathbf{m}_{k-1}^i) \quad (25)$$

$$= \mathbf{z}_{2D,k}^i - \pi({}_{k-1}^W\mathbf{G}_k {}^W\mathbf{m}_{k-1}^i), \quad (26)$$

where ${}_{k-1}^W\mathbf{G}_k = {}^W\mathbf{X}_k^{-1} {}_{k-1}^W\mathbf{H}_k$. Since Eq. (26) is in the same form as Eq. (24), we can solve for ${}_{k-1}^W\mathbf{G}_k$ in the same fashion, and the object motion:

$${}_{k-1}^W\mathbf{H}_k = {}^W\mathbf{X}_k {}_{k-1}^W\mathbf{G}_k$$

can be directly recovered. As before, RANSAC is used to detect outliers and update the inlier tracks in the current frame. Building on [15], we enhance the initial object motion estimation and refine the inlier tracks through two additional steps, detailed in Sec. VI-B4 and Sec. VI-B5, respectively. The method proposed in Sec. VI-B4 was used in [15] to improve the estimation and tracking. With the addition of Sec. VI-B5 our method augments this process to further improve the estimation and identify outliers. At each stage of the refinement process, the set of inlier tracks is updated, significantly improving the robustness of the estimation. The three-steps outlined assumes that the motion of each object is independent, allowing DynoSAM to parallelize the object motion estimation process by handling each object instance in a separate thread.

4) *Joint Optical-Flow Refinement:* Following the work of [15], [51], the optical flow is jointly refined with the camera pose and object motions. This step is important to ensure robust and accurate feature tracking on both static and dynamic features. The measured flow and the associated SE(3) transformation are jointly refined by reformulating the re-projection errors from Eq. (26) and Eq. (24) in terms of the measured flow:

$$\begin{aligned} \mathbf{r}_{f,H} &= \mathbf{z}_{2D,k-1} + \mathbf{f}_{k-1,k} - \pi({}_{k-1}^W\mathbf{G}_k {}^W\mathbf{m}_{k-1}^i) \\ \mathbf{r}_{f,X} &= \mathbf{z}_{2D,k-1} + \mathbf{f}_{k-1,k} - \pi({}^W\mathbf{X}_k^{-1} {}^W\mathbf{m}^i) \end{aligned} \quad (27)$$

where $f_{k-1,k}$ defines the optical flow between two keypoints:

$$f_{k-1,k} = \mathbf{z}_{2D,k} - \mathbf{z}_{2D,k-1}.$$

Given 3D-2D point correspondences, the resulting non-linear least squares problem is formulated using a factor graph:

$$\{\theta, \mathbf{f}_{k-1,k}\} = \underset{\{\theta, \mathbf{f}_{k-1,k}\}}{\operatorname{argmin}} \left(\sum_i^N \rho_h \|\mathbf{r}_{f,\theta}\|_{\Sigma_f}^2 + \sum_i^N \|\mathbf{r}_0(f)\|_{\Sigma_0}^2 \right), \quad (28)$$

where θ represents either ${}^W\mathbf{X}_k$ camera pose or ${}_{k-1}\mathbf{G}_k$ in the case of object motion estimation. Depending on θ , $\mathbf{r}_{f,\theta}$ is either $\mathbf{r}_{f,X}$ or $\mathbf{r}_{f,H}$, as in Eq. (27). The covariance matrix $\Sigma_0 \in \mathbb{R}^{2 \times 2}$ associated with the flow prior $\mathbf{r}_0(f)$ is diagonal and associated with the measured optical-flow. As each object moves independently, we construct and solve this optimization problem in parallel per object. Through this joint optimization, we refine temporal point associations improving feature tracking and pose estimation. During optimization, we enhance robustness by eliminating additional outliers, specifically those exhibiting large re-projection errors.

5) *Object Motion Refinement*: The object motion estimates can be further refined by employing the rigid-body motion model defined in Eq. (17) to formulate an additional nonlinear least-square optimization problem that directly estimates the object motion ${}_{k-1}{}^W\mathbf{H}_k$. In contrast to the preceding step, which uses a 2D pixel error, this residual function is based on 3D point errors. Empirically, we have observed that this 3D-based approach significantly enhances estimation accuracy and removes additional outliers not previously identified.

Using the motion estimate from the previous steps as an initial estimate, the *motion only refinement graph* shown in Fig. 6 is build per object and defines the nonlinear least-squares problem:

$$\theta_k^{\text{MAP}} = \underset{\mathbf{H}}{\operatorname{argmin}} \left(\|\mathbf{r}_0({}^W\mathbf{X}_{k-1})\|_{\Sigma_0}^2 + \|\mathbf{r}_0({}^W\mathbf{X}_k)\|_{\Sigma_0}^2 \right) \quad (29.0)$$

$$+ \sum_{\mathcal{D}_{k-1}^j \cup \mathcal{D}_k^j} \|\mathbf{r}_{2D,R}\|_{\Sigma_{2D,R}}^2 \quad (29.1)$$

$$+ \sum_{\mathcal{D}_{k-1}^j \cup \mathcal{D}_k^j} \|\mathbf{r}_{3D,H}\|_{\Sigma_{3D,H}}^2 \right), \quad (29.2)$$

The Levenberg–Marquardt solver is used to obtain the final object motion estimate ${}_{k-1}{}^W\mathbf{H}_k$. Based on Eq. (24), Eq. (29.1) forms projection factors with an associated covariance matrix $\Sigma_{2D,R} \in \mathbb{R}^{2 \times 2}$, connecting dynamic points and the observing camera poses at time-step $k-1$ and k . Eq. (29.2) describes the 3D motion residual of Eq. (17) and connects the common motion with each tracked landmark. $\Sigma_{3D,H} \in \mathbb{R}^{3 \times 3}$ is the associated covariance matrix. Eq. (29.0) represents prior factors on the camera poses. Since this refinement step focuses exclusively on improving object motion estimation, and not camera pose, a strong prior on the camera poses are used during optimization. This is achieved by assigning the covariance matrix $\Sigma_0 \in \mathbb{R}^{6 \times 6}$ with very small values ($\sigma = 0.0001$ in our experiments).

C. Back-end

The back-end fuses static and dynamic measurements to jointly estimate the trajectory of the camera and each object as well as a global map of static and dynamic points. Our

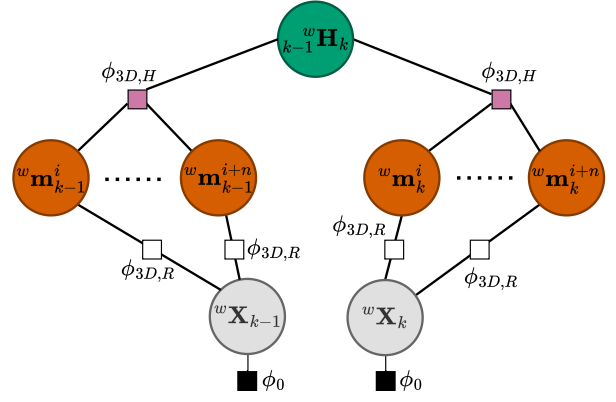


Fig. 6: Factor graph representing the motion only refinement graph. For each object $j \in \mathcal{J}_k$, the motion is refined by minimizing the 3D motion residual using measurements of points tracked between $k-1$ and k . In our example we show the dynamic points in orange, the motion in green, the 3D motion residual in purple and the re-projection factors in white. We only show two sets of points i and $i+n$, while in reality there would be n motion factors.

back-end allows different Dynamic SLAM formulations to be selected and used for estimation. Full-batch and sliding window optimization methods are provided.

As discussed in [18], the optimization problem for Dynamic SLAM can be formulated in various ways, employing different sets of variables and objective functions. The choice of formulation plays a crucial role in determining the system's accuracy. In this work, we present and evaluate two world-centric estimation approaches, described in Sec. V, as integral components of DynoSAM.

To enable the seamless use of the DynoSAM pipeline for downstream tasks, the system's output must be clearly defined and consistently maintained, regardless of the specific formulation used to solve the estimation problem. As previously discussed, formulations can represent objects using different state variables (poses or motions as shown in this work) and in different frames of reference (locally as in [21] or in the camera frame [17]). Therefore, a post-estimation processing step is required to convert all estimated states into a common representation to ensure that results can be directly compared, evaluated using consistent metrics, and readily used by downstream applications. Our framework facilitates this by clearly defining a set of outputs:

$$\mathcal{O}_k = [{}^W\mathbf{X}_k, {}_{k-1}{}^W\mathbf{H}_k, {}^W\mathcal{L}_k, {}^W\mathcal{M}_k] \quad k \in \mathcal{K} \quad (30)$$

regardless of the formulation. If the formulation used does not directly estimate a required output element, it must be computed directly from the available information. This behavior is enforced in DynoSAM's back-end implementation via clear abstraction layers.

D. Implementation

The camera pose and motion estimation algorithms described in the previous sections are implemented in C++. GTSAM 4.2 [54] is used for all non-linear optimization problems which are solved using Levenberg–Marquardt. For all experiments, unless otherwise specified (Sec. VII-E), full-batch optimization is used.

At each time-step, the back-end component constructs a system by incorporating new factors and variables based on inputs from the front-end, which consists of initial estimates for the camera pose ${}^W\mathbf{X}_k$, per-object motions ${}_{k-1}{}^W\mathcal{H}_k$ and a set of visual measurements \mathcal{Z}_k . The system is then optimized, and the resulting estimates are processed to generate the output \mathcal{O}_k . Compared to a typical static SLAM system, the graph format of the input data is significantly more complex, and, depending on the formulation, may contain ternary Eq. (17) and quaternary edges Eq. (21).

For both formulations discussed in Sec. V, the system defines new variables at each time-step for ${}_{k-1}{}^W\mathbf{H}_k$ or ${}^W\mathbf{L}_k$ which represent the state of each object, and initializes them with values from the front-end where applicable. Each dynamic point measurement in $\mathcal{D}_{3D,k}$ contributes to constraining object states based on the observed camera pose(s) and its corresponding dynamic map point.

This combination of factors and state variables results in a Dynamic SLAM problem that DynoSAM manages and constructs efficiently and flexibly, despite the significant increase in graph size and associated bookkeeping when compared to the classical static SLAM problem. DynoSAM achieves this by decoupling the measurement bookkeeping from the implementation of individual Dynamic SLAM formulations through abstraction layers, as mentioned in the previous section. This design choice dramatically simplifies the implementation of new formulations, allowing researchers to easily experiment with different approaches. Further technical details regarding graph construction and the abstractions used are available in our documented open-source software¹.

Finally, we note that loop closure has not been incorporated into the system and is beyond the scope of this work.

VII. EXPERIMENTS

Our framework has been rigorously tested on indoor and outdoor datasets featuring diverse dynamic objects. We present results of camera trajectories and object motions using full-batch optimization, as well as the performance using sliding window optimization (Sec. VII-E). In particular, we compare the accuracy of DynoSAM’s World-Centric Motion and Pose Estimator (henceforth referred to as DynoSAM Motion and DynoSAM Pose) against MVO [17], VDO-SLAM [15], ClusterSLAM [24] and DynaSLAM II [21]. Our evaluation is conducted using the metrics outlined in Sec. VII-A and provides a comprehensive assessment of these systems. All evaluation metrics are included in our open-source framework and are based on the implementation of *evo* [64]. Of the systems we compare against, only VDO-SLAM [15] provides an open-source implementation of their pipeline which we use to directly obtain the results reported. In the case of MVO, their pipeline’s raw output data was provided by the authors, allowing all metrics to be used during evaluation. Cluster-SLAM [24] uniquely reports accumulated average camera and object pose errors over all sequences, instead of individual results per sequence. We therefore report an accumulated average error to facilitate comparison with their system and

use the values reported in [24]. We use the camera pose errors of DynaSLAM II as reported in [21]. Due to limited reported results and the lack of object ID associations between their results and our dataset, we exclude DynaSLAM II object errors from our comparisons.

A. Metrics

This section explains the metrics used in our DynoSAM framework to evaluate the accuracy of pose and motion estimations for camera and objects. For camera localization accuracy, we employ conventional evaluation methods that assess the camera trajectory and motions. However, the evaluation of object pose and motion remains challenging as each object body-fixed reference frame is defined arbitrarily by each and any dataset. As explained in Sec. IV-A, different local references on the same rigid-body object will experience different local motions and have different trajectories. In addition, the information on where the object local reference frame is on each object in the ground truth is often missing from most datasets, as is the ground truth object motion. Therefore, in this section we discuss in detail the characteristics of each metric DynoSAM employs, especially those agnostic to reference frame definitions.

We evaluate the accuracy of camera pose and motion estimation using a combination of standard metrics, e.g. Absolute Pose Error (APE), Absolute Trajectory Error (ATE) and Relative Pose Error (RPE) as defined by Sturm *et al.* [65]. For every error metric \mathbf{E} for a $\text{SE}(3)$, we compute and report the root-mean-squared error (RMSE) of the translation and rotation component separately:

$$\text{RMSE}(e) = \sqrt{\frac{1}{n(\mathcal{K})} \sum_{k \in \mathcal{K}} \|e_k\|^2}, \quad (31)$$

where e_k is a scalar error at each time-step k throughout a sequence. The scalar translational error is the L_2 norm of the translation component $\text{trans}(\mathbf{E}_k)$, and the rotational error is the angle of the rotation component $\text{rot}(\mathbf{E}_k)$.

Given a ground truth transformation $\mathbf{M}_{\text{gt},k} \in \text{SE}(3)$ and a corresponding reference estimate $\mathbf{M}_k \in \text{SE}(3)$ at time $k \in \mathcal{K}$, the APE at this time-step is defined as:

$$\text{APE}_k = \mathbf{M}_{\text{gt},k}^{-1} \mathbf{M}_k \in \text{SE}(3). \quad (32)$$

ATE is calculated as the root-mean-squared error (RMSE) of the translation component of the APE:

$$\text{ATE} = \text{RMSE}(\text{trans}(\text{APE}_k)), \quad (33)$$

and is commonly used to evaluate the absolute camera trajectory error [3], [21], [35].

We use the relative pose error (RPE) metric for further pose evaluation. RPE is the RMSE of the difference in relative poses between consecutive frames, computed for translation and rotation separately:

$$\begin{aligned} \text{RPE}_t &= \text{RMSE}(\text{trans}(\text{RPE}_k)) \\ \text{RPE}_r &= \text{RMSE}(\text{rot}(\text{RPE}_k)), \end{aligned} \quad (34)$$

¹<https://github.com/ACFR-RPG/DynOSAM>

TABLE I: Quantitative evaluations of camera trajectory for all experiments.

		KITTI										Outdoor Cluster					OMD
		00	01	02	03	04	05	06	18	20	L1	L2	S1	S2	avg.	S4U	
ATE(m)	DynaSLAM II	1.29	2.31	0.91	0.69	1.42	1.34	0.19	1.09	1.36	-	-	-	-	-	-	
	VDO-SLAM	3.37	6.74	2.47	2.12	4.53	3.8	0.45	9.94	7.82	-	-	-	-	-	0.19	
	ClusterSLAM	-	-	-	-	-	-	-	-	-	-	-	-	-	0.53	-	
	MVO	1.53	-	-	-	-	-	-	-	-	-	-	-	-	-	0.05	
	DynoSAM Pose	0.82	2.00	0.73	0.82	2.01	1.58	0.31	1.84	1.26	0.89	0.84	0.25	0.52	0.63	0.11	
	DynoSAM Motion	0.82	2.00	0.73	0.82	2.01	1.58	0.31	1.84	1.26	0.1	0.84	0.26	0.52	0.51	0.11	
RPE _r (°)	DynaSLAM II	0.06	0.04	0.02	0.06	0.06	0.03	0.04	0.02	0.04	-	-	-	-	-	-	
	VDO-SLAM	0.08	0.05	0.03	0.03	0.06	0.03	0.1	0.03	0.04	-	-	-	-	-	0.77	
	ClusterSLAM	-	-	-	-	-	-	-	-	-	-	-	-	-	1.15	-	
	MVO	0.19	-	-	-	-	-	-	-	-	-	-	-	-	-	0.76	
	DynoSAM Pose	0.05	0.03	0.02	0.05	0.06	0.06	0.05	0.04	0.04	0.88	0.69	0.03	0.30	0.48	0.69	
	DynoSAM Motion	0.04	0.03	0.02	0.05	0.06	0.05	0.05	0.04	0.04	1.26	0.69	0.03	0.31	0.57	0.69	
RPE _t (m)	DynaSLAM II	0.04	0.05	0.04	0.04	0.07	0.06	0.02	0.05	0.07	-	-	-	-	-	-	
	VDO-SLAM	0.09	0.15	0.05	0.09	0.14	0.11	0.04	0.09	0.30	-	-	-	-	-	0.12	
	ClusterSLAM	-	-	-	-	-	-	-	-	-	-	-	-	-	1.10	-	
	MVO	0.07	-	-	-	-	-	-	-	-	-	-	-	-	-	0.004	
	DynoSAM Pose	0.04	0.04	0.03	0.05	0.07	0.05	0.01	0.04	0.04	0.25	0.51	0.008	0.02	0.2	0.006	
	DynoSAM Motion	0.04	0.04	0.03	0.05	0.06	0.05	0.01	0.04	0.02	0.64	0.51	0.008	0.02	1.2	0.006	

where at each time-step k :

$$\text{RPE}_k = (\mathbf{M}_{\text{gt},k-1}^{-1} \mathbf{M}_{\text{gt},k})^{-1} (\mathbf{M}_{k-1}^{-1} \mathbf{M}_k). \quad (35)$$

For evaluation of camera pose we set $\mathbf{M} = {}^W \mathbf{X}_k$ to compute ATE and RPE. We assess object RPE by setting $\mathbf{M} = {}^W \mathbf{L}_k$. This metric allows us to easily compare with other state-of-the-art Dynamic SLAM systems [24], [21], [35], [17]. Note that the RPE definition commonly employed here is different from the relative translation and rotation errors used by some classic visual SLAM systems to evaluate the accumulated camera pose errors over distance traveled [66], [3]. Because the poses and trajectory of an object change based on where its local reference frame is defined, which differs for each system, we do not evaluate APE or ATE for objects.

It is also vital to understand the accuracy of our estimated object motion. We evaluate the local motion of each object using the Motion Error ME. For each estimated observed motion ${}_{k-1}^W \mathbf{H}_k$ we calculate the local motion using the object pose ground truth:

$${}^W \mathbf{L}_{\text{gt},k-1}^{-1} \mathbf{H}_k = {}^W \mathbf{L}_{\text{gt},k-1}^{-1} {}_{k-1}^W \mathbf{H}_k {}^W \mathbf{L}_{\text{gt},k-1} \quad (36)$$

and define the motion error for each time-step k :

$$\text{ME}_k = {}_{k-1}^L \mathbf{H}_{\text{gt},k}^{-1} {}_{k-1}^L \mathbf{H}_k, \quad (37)$$

As before, we report the RMSE for the translation and rotation error throughout the sequence for all objects:

$$\begin{aligned} \text{ME}_t &= \text{RMSE}(\text{trans}(\text{ME}_k)) \\ \text{ME}_r &= \text{RMSE}(\text{rot}(\text{ME}_k)). \end{aligned} \quad (38)$$

We include only objects that have been observed for at least 3 consecutive frames, i.e. having at least 2 motions in our reported results.

From Eq. (7) and our earlier definitions of motion, we highlight that RPE and ME are *similar* metrics, but with

nuanced differences:

$$\text{RPE}_k = ({}^W \mathbf{L}_{\text{gt},k-1}^{-1} {}^W \mathbf{L}_{\text{gt},k})^{-1} ({}^W \mathbf{L}_{k-1}^{-1} {}^W \mathbf{L}_k) \quad (39.0)$$

$$= {}_{k-1}^L \mathbf{H}_{\text{gt},k}^{-1} {}_{k-1}^L \mathbf{H}_k \not\cong \text{ME}_k. \quad (39.1)$$

The difference between Eq. (37) and the RPE component of Eq. (39.0) lies in the reference frame of the estimated motions: ME uses the *ground truth* object frame ${}^L \mathbf{H}_{\text{gt},k-1}$ specified by the pose ${}^W \mathbf{L}_{\text{gt},k-1}$ while RPE uses the *estimated* object frame.

Our framework includes the ME and RPE metrics as both are relevant to understanding the quality of the estimated motion and facilitate comparison with a wider range of systems. While RPE is a common criteria employed by most state-of-the-art Dynamic SLAM systems [24], [21], [17], this metric is not invariant to where the estimated object reference frame is defined. By comparison, ME is made agnostic to the estimated frame by using the ground truth object frame as its reference, which ensures that any resulting error is purely a result of error in the *motion* and not also in the pose. However, RPE remains a useful metric to evaluate the resulting trajectory. It should be noted that, when the Dynamic SLAM system only estimates object motions, e.g. DynoSAM Motion Estimator, the object pose ${}^W \mathbf{L}_k$ must be computed by propagating the initial object pose ${}^W \mathbf{L}_s$ using the estimated motions:

$${}^W \mathbf{L}_k = {}_{k-1}^W \mathbf{H}_k \dots {}_s^W \mathbf{H}_{s+1} {}^W \mathbf{L}_s. \quad (40)$$

In this case, RPE not only accumulates the drift in motion estimation, but also sums them up throughout the object observation in the RMSE calculation.

To ensure our framework performs fair and accurate evaluation, it is vital that we correctly align the camera and object frames with their respective ground truth frames. For camera pose evaluation, the estimated and ground truth states share a common and well defined reference frame, making alignment and comparison simple. During experiments we align the ground truth origin to the estimated trajectory using Umeyama's method [67]. To facilitate a valid evaluation of

RPE, we define the start of each object trajectory using the first ground truth object pose, i.e. Eq. (40) to ensure a common object frame definition. To guarantee that the estimated objects also share the same world frame, we calculate ${}_{k-1}^W \mathbf{H}_{\text{gt},k}$ and ${}^W \mathbf{L}_{\text{gt},k}$ directly from the dataset using the newly aligned ground truth odometry. This ensures that both the world and object frames are defined correctly for each sequence, facilitating a valid comparison.

B. Datasets

We evaluate our system on the real-world KITTI tracking dataset [66], OMD [22] and the outdoor datasets provided by ClusterSLAM [24]². Each dataset was selected specifically as they contain ground truth object pose information in addition to the camera pose, allowing ground truth object motion to be extracted for each object.

ClusterSLAM provides 10 simulated dynamic sequences, 4 of which present driving sequences similar to KITTI and include numerous instances of dynamic vehicles. These sequences are denoted as the ‘outdoor’ sequences by ClusterSLAM [24], hence we refer to them as the *Outdoor Cluster* dataset in this paper. These datasets provide diverse and complex scenes, including multiple objects, partial and full occlusions, and semi-rigid objects like cyclists. These challenges test DynoSAM’s ability to handle real-world scenarios. However, in most of these scenarios the objects all experience relatively constant motion.

To fully assess DynoSAM’s ability to estimate complex dynamics, we also evaluate the motion estimation results of our system using the *swinging_4 unconstrained* (S4U) sequence of the OMD. This sequence features four swinging cubes with unconstrained and unpredictable motion in an enclosed environment. The camera motion in this sequence also differs from KITTI and Outdoor Cluster in that it mimics hand-held camera motion with complex rotations. While the OMD contains other sequences, the S4U sequence exhibits the most challenging motion of the dataset and facilitates comparison to MVO. While MVO also utilizes the *occlusion_2 unconstrained* sequence to assess their occlusion handling capabilities, this specific focus is outside the scope of our work. Consequently, we do not evaluate our framework on this sequence.

We use a processed version of the KITTI tracking dataset which contains ground truth camera and object pose, as well as object motions, per frame. The Outdoor Cluster sequences use CARLA [68] as the simulation engine where ground truth object states and camera poses can be obtained directly. OMD uses a Vicon motion capture system to obtain ground truth trajectories of the camera and objects; full details of the experimental setup can be found in [22].

To ensure valid evaluation, we pre-process these datasets offline to produce input images as well as ground truth camera and object poses/motions. For the S4U (OMD) sequence, we use color thresholding to create semantic instance masks, as the ‘square box’ class is absent from YOLO’s training data. For KITTI, we utilize pre-computed depth maps to obtain

²The datasets are provided in addition to the paper and can be found at <https://huangjh-pub.github.io/page/clusterslam-dataset/>

dense depth information. For all other datasets, we calculate per-pixel depth, optical flow, and semantic segmentation as outlined in Section VI-A. To maintain consistency and reproducibility, we save the processed input images to file and during evaluation load these images to guarantee identical input data for each run. To isolate the performance of our back-end estimation, we serialize the front-end output to file. This allows us to feed the same data association, measurements, and initial estimates to each DynoSAM formulation, allowing the impact of each approach to be accurately assessed. We provide custom parsers in C++ and Python to load and save the output of our front-end.

C. Camera Pose Error

The accuracy of DynoSAM’s camera pose estimation is evaluated using RPE and ATE as shown in Table I, where we outperform the state-of-the-art systems or achieve comparable results. Both DynoSAM back-ends (pose and motion estimators) demonstrate almost identical performance, which is expected as they share a common visual odometry formulation.

DynoSAM shows significant improvement over VDO-SLAM [15] on all sequences tested, and outperforms ClusterSLAM [24] in the Outdoor Cluster experiments, achieving lower average errors in both translation and rotation. On the KITTI dataset, DynoSAM performs better than DynaSLAM II [21] in relative translation and demonstrate comparable accuracy in rotation estimation. DynaSLAM II produces better results than DynoSAM in Sequences 03–18 in ATE, however, the difference is minor. We believe this difference is due to the different underlying camera pose estimation algorithm employed by each system. Compared to MVO [17], we achieve similar performance on the OMD and demonstrate superior performance on KITTI.

D. Object Motion and Pose Errors

Table II compares the pose and motion estimators implemented in DynoSAM and demonstrate that both estimators achieve state-of-the-art object motion and pose estimation when compared to existing systems. Of the two DynoSAM formulations presented, the motion estimator is 40% more accurate in ME_t and 135% more accurate in ME_r on a per-sequence basis compared to the pose estimator. Furthermore, this method estimates the object trajectory more accurately as indicated by the lower RPE. While the motion estimator produces more accurate results it should be noted that both estimators as part of the DynoSAM framework consistently outperform other systems in all experiments. Table II also demonstrates the state-of-the-art performance of our proposed formulations when compared to existing methods. We further summarize the average percentage improvement of the DynoSAM motion estimator (the more accurate of the two formulations) over existing systems in Table III, highlighting our frameworks consistent accuracy. These tables demonstrates clear improvement over state-of-the-art methods across RPE and ME metrics.

Compared to VDO-SLAM [15], our framework exhibits superior accuracy in object motion and pose estimation. This

TABLE II: Quantitative evaluations of average object motions and poses for all experiments.

		KITTI										Outdoor Cluster				OMD
		00	01	02	03	04	05	06	18	20	L1	L2	S1	S2	avg.	S4U
ME _r (°)	VDO-SLAM	1.38	2.15	1.68	0.39	2.8	0.48	2.8	0.36	0.49	-	-	-	-	-	0.96
	ClusterSLAM	-	-	-	-	-	-	-	-	-	-	-	-	-	-	-
	MVO	3.36	-	-	-	-	-	-	-	-	-	-	-	-	-	1.1
	DynoSAM Pose	1.23	0.91	0.95	0.27	0.76	0.56	2.8	1.15	0.39	4.2	0.42	2.88	1.02	-	1.6
ME _t (m)	DynoSAM Motion	1.29	0.86	1.06	0.26	1.01	0.49	0.39	0.6	0.33	0.65	0.40	0.52	0.44	-	0.71
	VDO-SLAM	0.11	0.35	0.43	0.15	0.38	0.19	0.11	0.16	0.08	-	-	-	-	-	0.02
	ClusterSLAM	-	-	-	-	-	-	-	-	-	-	-	-	-	-	-
	MVO	0.27	-	-	-	-	-	-	-	-	-	-	-	-	-	0.03
RPE _r (°)	DynoSAM Pose	0.09	0.40	0.73	0.15	0.1	0.14	0.22	0.31	0.39	1.65	16.6	0.34	0.64	-	0.07
	DynoSAM Motion	0.15	0.34	0.4	0.15	0.09	0.13	0.11	0.20	0.05	2.19	1.86	0.037	0.37	-	0.02
	VDO-SLAM	-	-	-	-	-	-	-	-	-	-	-	-	-	-	-
	ClusterSLAM	-	-	-	-	-	-	-	-	-	-	-	-	-	10.3	-
RPE _t (m)	MVO	2.7	-	-	-	-	-	-	-	-	-	-	-	-	-	3.13
	DynoSAM Pose	1.27	0.89	1.02	0.27	0.74	0.6	3.00	1.38	0.37	4.6	12.87	2.87	0.57	5.22	4.1
	DynoSAM Motion	1.38	0.80	1.06	0.27	1.04	0.62	2.74	1.16	0.33	0.73	0.40	0.53	0.26	0.48	3.2

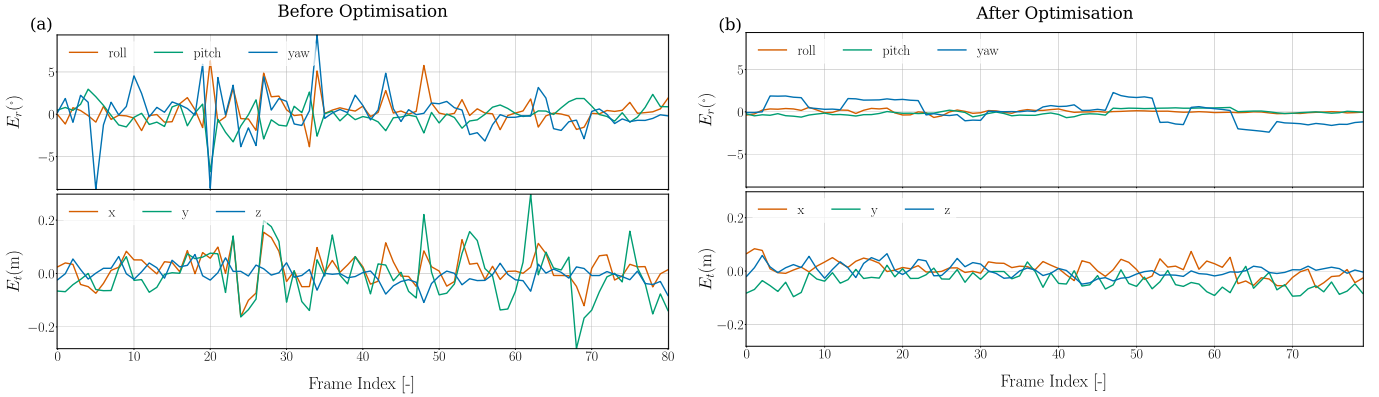


Fig. 7: Example of per-frame ME before (a) and after (b) optimization. Translation and rotation errors are shown individually; along the top and bottom rows respectively. Here we show the errors for Object 2 (cyclist) on KITTI 00 using the motion estimator.

TABLE III: Average percentage improvement of DynoSAM Motion estimator compared to state-of-the-art Dynamic SLAM systems. Green cell blocks indicate improvement over existing systems while red blocks indicate relatively worse accuracy.

	VDO-SLAM [15]	ClusterSLAM [24]	MVO [17]
ME _r (°)	+28 %	-	+49 %
ME _t (m)	+9 %	-	+39 %
RPE _r (°)	-	+95 %	-9 %
RPE _t (m)	-	+84 %	+12 %

improvement is particularly pronounced on the OMD, where DynoSAM is 34 % more accurate in rotation and 21 % in translation errors, as measured by the ME metric. Evaluation results presented in Table II demonstrate the superior accuracy of the proposed framework across most evaluated sequences. However, VDO-SLAM exhibits better performance on two KITTI datasets, specifically sequences 05 and 18. While the performance difference is marginal for KITTI 05, a more pronounced discrepancy is observed for KITTI 18. This latter sequence depicts a highway driving scenario characterized by

TABLE IV: ME error per object on the OMD (S4U), comparing our motion estimator with MVO and VDO-SLAM. The object ID's reported here correspond with the following object's in the dataset: 1 - top left, 2 - top right, 3 - bottom left, 4 - bottom right.

Object	MVO [17]		VDO-SLAM [15]		DynoSAM	
	ME _r (°)	ME _r (m)	ME _r (°)	ME _r (m)	ME _r (°)	ME _r (m)
1	0.542	0.0169	1.256	0.0243	1.138	0.0214
2	0.843	0.0269	0.770	0.0234	0.544	0.0233
3	1.648	0.0232	0.907	0.0148	0.443	0.0086
4	0.854	0.0309	0.927	0.0293	0.474	0.0291

an extended camera trajectory and frequent vehicle stops and starts due to traffic congestion. We have observed that our system generates substantially longer object tracks compared to VDO-SLAM, which is likely the source of the degraded performance. We envisage this error will disappear with the use of sliding-window optimization.

When compared to ClusterSLAM [24], Table III demonstrates that our framework is at least 84 % more accurate in both rotation and translation. As ClusterSLAM only reports accumulated error, we additionally report the accumulated

TABLE V: Average object ME comparison of full-batch vs. sliding window approach on the KITTI and OMD datasets.

	Full-Batch		Sliding Window	
	$ME_r(^{\circ})$	$ME_t(m)$	$ME_r(^{\circ})$	$ME_t(m)$
KITTI 00	1.11	0.072	1.039	0.065
OMD (S4U)	0.729	0.022	0.659	0.021

object motion error based on DynoSAM’s per-sequence errors in Table II. While this particular error representation makes it hard to perform further comparisons, the significant difference in accuracy between the two systems strongly suggests DynoSAM’s superior performance.

Table III demonstrates that DynoSAM outperforms MVO [17] across all metrics. Our framework is particularly accurate in translation with a 39 % improvement in ME and 12 % improvement in RPE. The one exception is in RPE_r on the OMD where MVO is more accurate by a small margin. This likely explains the relatively worse relative rotation error seen in Table III. However, our method actually outperforms MVO on a per-object basis as shown in Table IV, which reports the ME for each object in the S4U sequence and reinforces the accuracy of our system even on this challenging datasets. This table also show that our framework additionally outperforms VDO-SLAM per-object.

Finally, Fig. 7 compares the per-frame ME before and after optimization on Object 2 from KITTI 00. By examining the results on a per-frame basis, we show that our framework produces accurate estimation across the entire trajectory of the object. Comparing the errors before and after optimization highlight the superior accuracy and smoothness of the back-end’s motion estimation compared to the initial-estimates from the front-end, underscoring the critical role of back-end in achieving accurate object motion estimation over the full object trajectory.

It is clear our framework is able to achieve highly accurate motion estimation in both indoor and outdoor environments and demonstrates state-of-the-art performance compared to other systems. On average, both presented back-end formulations perform comparably, however we demonstrate that the motion estimator is a more reliable method.

E. Sliding Window Optimisation

Up to now we have presented experiment results of a full-batch solution, where all measurements are incorporated into a single optimization problem. While accurate, this approach is computationally expensive and unsuitable for online use. Furthermore, object motions often exhibit increasing independence over extended time horizons, even for objects with strong motion priors, such as vehicles on highways, thus making long-term trajectory optimization potentially unnecessary. We therefore implemented a sliding-window approach as a preliminary investigation. This approach creates smaller, more efficient batch estimation problems every w frames, initializing overlapping variables with values from the previous window. Fig. 8 compares our full-batch and sliding window approaches, reporting the the average ME for each object *per frame* on the KITTI 00 and OMD sequences. For this

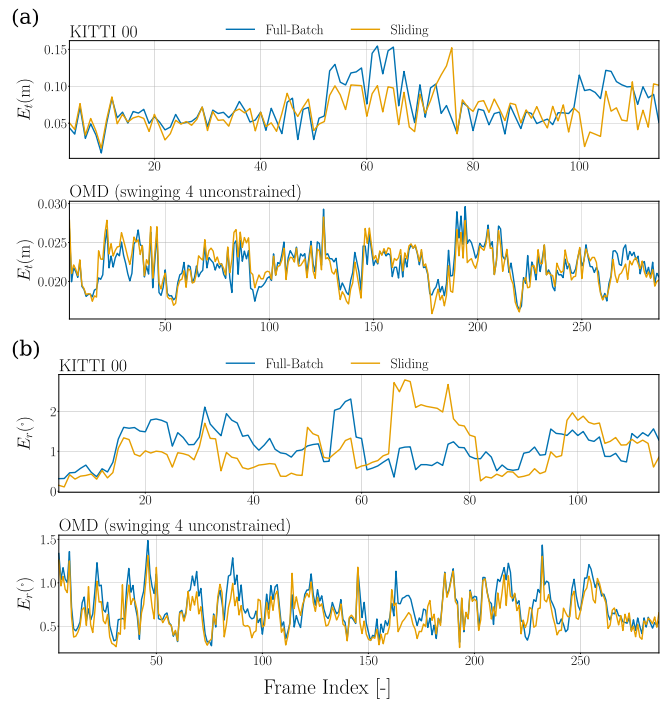


Fig. 8: Object motion errors comparing full-batch vs. sliding window. We take the ME for each object *per frame* and report the average in translation (a) and rotation (b). The motion estimator is used for both sets of results.

experiment we used a window size of 20 frames and a 4 frame overlap between windows, although these parameters are tunable. As shown in Table V the sliding-window method achieves comparable, albeit slightly lower, average per-frame error than full-batch on both sequences. However, full-batch demonstrates slightly more consistent accuracy, as seen in the KITTI 00 sequence between frames 70 and 85, where the sliding window experiences a larger error increase at a window overlap, potentially a result of poor front-end tracking at that frame. These preliminary results suggests that incorporating motion data over a receding time horizon remains beneficial.

F. Computation Time

Fig. 9 presents the runtime breakdown for each module in the front-end. The feature tracking module, which includes feature extraction, matching, and geometric verification, requires less than 50 ms. The motion estimation module, responsible for estimating the camera pose and all object motions per frame, averages 100 ms to produce all estimates. However, the majority of processing time is spent on the object motion refinement component, which takes approximately ≈ 250 ms per object to solve the nonlinear optimization problem. The runtime of this component depends heavily on the number of points involved in the optimization, leading to significant variation in processing times.

In our experiments, the time required for full-batch optimization ranges from 80 s to 700 s, depending on the size of the constructed factor graph. These values align with those reported in [18]. While the full-batch optimization may not meet real-time requirements, it is important to note that

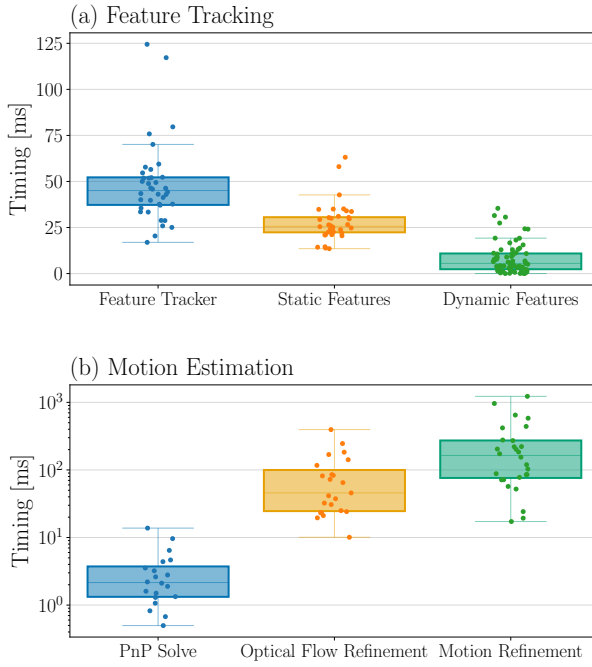


Fig. 9: Runtime breakdown of DynoSAM’s front-end. (a) shows the timing for feature tracking and (b) shows the timing per each estimation module discussed in Sections VI-B2, VI-B3 (PnP Solve), VI-B4 (Joint Optical Flow) and VI-B5 (3D Motion Refinement). Note that (b) uses log-scale for the timing axes.

practical applications typically rely on much smaller sliding window optimizations in the back-end. This approach significantly reduces computational demands and improves efficiency for online operation. Future work will focus on enhancing the efficiency of the back-end, including techniques such as conditional variable elimination [69], to better support real-time applications.

VIII. DOWNSTREAM TASKS

The proposed Dynamic SLAM system accurately estimates the motions of dynamic objects, as validated in Section VII. By eliminating the need for prior knowledge of motion models or object categories, our framework enables a range of downstream applications. This section explores how accurate motion estimation, produced by our pipeline, can facilitate dynamic object reconstruction and trajectory prediction, both of which are crucial for navigation systems.

A. Dynamic Object Reconstruction

Many reconstruction systems assume the environment to be static and rigid [70], [71], as with many traditional SLAM systems. Leveraging DynoSAM for dynamic object segmentation and motion estimation, we have developed DynORecon [8], a reconstruction system that focuses on incrementally mapping dynamic rigid-body objects. DynORecon employs a submap structure to separate the reconstruction of each dynamic object from the static map, ensuring that object motion does not leave any residual artifacts in the static map.

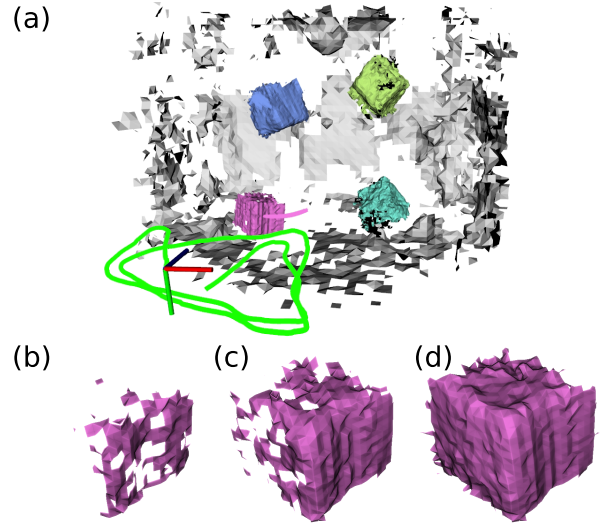


Fig. 10: One of our downstream applications, DynORecon [8], incrementally builds up surface mesh reconstructions of both dynamic objects and static background in the OMD experiment [22]. (a): a visualization of dynamic object meshes and their trajectories (uniquely coloured) as well as the static background (grey), in addition to camera pose and trajectory (green); (b-d): the incrementally constructed mesh of Object 3.

The accurate motion estimation from DynoSAM facilitates an easy and efficient integration of new object measurements into each existing object reconstruction while maintaining object rigidity. Based on Eq. (10), applying ${}_{k-1}^W \mathbf{H}_k$ as estimated by DynoSAM to all points on the object guarantees a consistent motion from time-step $k-1$ to k . Similarly, Eq. (2) and Eq. (4) show that the same motion can consistently transform any reference frame fixed to the object. Similar to the treatment of object pose in Sec. V-B and Sec. V-C, we can define an arbitrary reference frame that is rigidly attached to the object body without any prior knowledge on its pose, and use ${}_{k-1}^W \mathbf{H}_k$ to move this body-fixed frame with respect to the global world frame. This allows us to express all object points in the body-fixed frame, ${}^L \mathbf{m}$, where they are static and time-invariant with respect to their local frame. This representation allows new observations to be integrated into each object reconstruction while remaining consistent with previous measurements [8].

Fig. 10 presents an example of DynORecon incrementally constructing all 4 dynamic objects (free-floating cubes) in addition to the static background using DynoSAM’s estimations in the OMD experiment [22]. As shown in Fig. 10 (b-d), accurate motion estimations from the upstream Dynamic SLAM system enables a consistent incremental surface reconstruction as the object undergoes complex movement. Building up a correct representation of dynamic objects, as more of them are observed, provides a more comprehensive understanding of moving obstacles in the scene, and is therefore beneficial to other robotic applications such as planning and navigation.

B. Object Trajectory Prediction

Trajectory prediction plays a key role in path planning and control in dynamic environments. Safer and more efficient

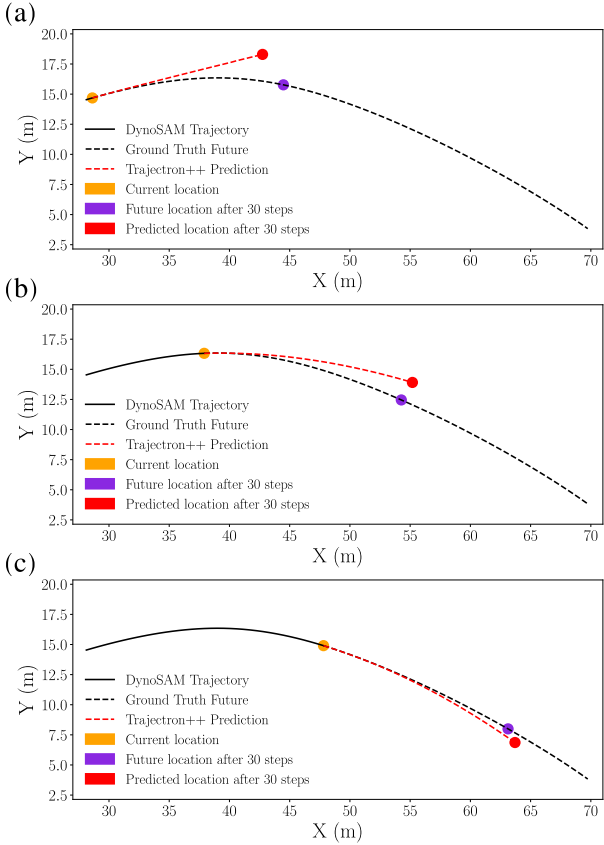


Fig. 11: Our second downstream application predicts object trajectories based on the output estimation of DynoSAM. We show inferred predictions compared to the future ground truth trajectory of Object 2 on KITTI 00. Three snapshots are shown along the object’s trajectory where (a) illustrates an initial prediction based on only 1 previous state and (b-c) show predictions based on 4 prior states.

navigation can be achieved by incorporating the anticipated future movements of dynamic objects into navigation algorithms [10], [72], [73], [74].

To test DynoSAM’s usability for a downstream task of trajectory prediction, we integrated our pipeline with Trajectron++ [75], a state-of-the-art trajectory prediction algorithm that uses a graph-structured recurrent model to forecast trajectories. Trajectron++ uses current and historical state information, including position, orientation and velocity for each object in the scene to generate real-time 2D predictions.

To provide this information for training and testing, we utilize the object trajectory data produced by DynoSAM. Object positions are taken directly from DynoSAM’s pose estimates ${}^W\mathbf{L}_k$, while velocities are calculated from the estimated motion ${}_{k-1}^W\mathbf{H}_k$. This processed Dynamic SLAM data is used to train and test Trajectron++ on the KITTI tracking dataset (Sec. VII-B). Our resulting testing dataset included 88 input instances from KITTI 00, while we used 406 training instances collected from the remaining seven KITTI sequences. To illustrate the effectiveness of our methods in a simplified setting, we limit our dataset to only include objects categorized as vehicles. We trained the base Trajectron++ model from scratch within the adaptive prediction framework [76].

Fig. 11 illustrates three snapshots of Object 2’s (cyclist) predicted trajectory at frames 67, 85 and 103 (a-c respectively).

On average, our predictions closely track the ground truth trajectory without exhibiting significant overshooting. These results, while preliminary, demonstrate that estimates from our Dynamic SLAM framework are accurate enough to be successfully used for trajectory predictions tasks. While the achieved predictions could be further improved by incorporating map generated by the DynORecon [8] module into Trajectron++; however, our predictions are already of high accuracy and could be leveraged to improve the motion planning module [9], [74], [77], or as informative motion priors within our Dynamic SLAM framework. Furthermore, the output from DynoSAM is 3D and future work will investigate trajectory forecasting algorithms that generate 3D predictions.

IX. LIMITATIONS AND FUTURE WORK

Our proposed method for Dynamic SLAM achieves high accuracy in motion and object trajectory estimation, but the back-end optimization is currently solved in full-batch mode at each step. While the front-end can deliver real-time performance, this paper highlights the vital role that the back-end plays in producing highly accurate and smooth object trajectories. Therefore, our immediate goal is to develop incremental solvers tailored to the specific challenges of the Dynamic SLAM problem.

Currently, our system uses a simplistic approach to modeling smooth object motion changes, relying on a constant motion constraint. As discussed in [17], this is akin to a constant velocity model, i.e. zero acceleration, which produces locally plausible motion but cannot capture motions of accelerating objects as accurately. Moving forward, we will be exploring more advanced motion models, potentially through learning, to better capture the short-term dynamics of each object.

The initial trajectory prediction results shown in Sec. VIII-B are promising; therefore we plan to further integrate these predictions into our system. Additionally, we aim to investigate how understanding the dynamics of each object can provide valuable feedback to enhance the SLAM pipeline and improve visual odometry.

Finally, we plan to leverage advanced transformer models such as SAM2 [78], [79] and FlowFormer [80] to improve scene understanding and explore new directions in Dynamic SLAM. We have designed DynoSAM with an emphasis on modularity and extensibility to facilitate such further research.

X. CONCLUSION

We have introduced DynoSAM, a cutting-edge, open-source framework for Dynamic SLAM that represents a significant advancement in the robotics field. By outlining the key theoretical concepts and formulations underpinning our approach, we provide a robust foundation for tackling the challenges of dynamic environments. DynoSAM offers a well-structured platform for implementing, testing, and evaluating Dynamic SLAM solutions, empowering researchers and practitioners to develop and benchmark innovative methodologies with greater ease and precision. Importantly, our implementation is designed for flexibility, with clearly defined interfaces between modules, facilitating integration with existing and new

methods. This contribution paves the way for more reliable and adaptable robotic systems in dynamic and complex settings.

This paper thoroughly examines state-of-the-art methods for the Dynamic SLAM problem and introduces a novel formulation tailored for real-world applications. We highlight the importance of framing the problem in terms of observed motion, which enables accurate estimation and recovery of object trajectories. Additionally, we evaluate all the discussed formulations and demonstrate that our framework outperforms existing systems in both motion estimation and visual odometry, setting a new benchmark for Dynamic SLAM solutions.

The paper also demonstrates DynoSAM’s effectiveness in downstream tasks such as motion prediction and 3D reconstruction. These capabilities collectively form the foundation for future dynamic object-aware navigation systems. With its user-friendly infrastructure and comprehensive evaluation suite, we aim for DynoSAM to serve as a robust platform for advancing research in Dynamic SLAM.

ACKNOWLEDGEMENTS

We would like to thank Kevin Judd and Jonathan Gammell for providing the results of MVO and their discussions. This research is funded with the support of ARIA Research and the Australian Government via the Department of Industry, Science, and Resources CRC-P program (CRCPXI000007).

APPENDIX

A. Rigid-body motion on points in the world frame

As discussed in the work of Zhang *et al.* [15], for any point on a rigid-body object measured in the world frame ${}^W \mathbf{m}_k$, there is the following equation:

$$\begin{aligned} {}^W \mathbf{m}_k &= {}^W \mathbf{L}_k {}^{L_k} \mathbf{m}_k \\ &= {}^W \mathbf{L}_{k-1} {}^{L_{k-1}} \mathbf{H}_k {}^{L_k} \mathbf{m}_k \end{aligned} \quad (41)$$

since ${}^W \mathbf{L}_k = {}^W \mathbf{L}_{k-1} {}^{L_{k-1}} \mathbf{H}_k$.

Based on the rigid-body assumption of this object, ${}^{L_k} \mathbf{m}_k$ is time-invariant, and therefore ${}^L \mathbf{m} = {}^{L_k} \mathbf{m}_k = {}^{L_{k-1}} \mathbf{m}_{k-1}$:

$$\begin{aligned} {}^W \mathbf{m}_k &= {}^W \mathbf{L}_{k-1} {}^{L_{k-1}} \mathbf{H}_k {}^{L_{k-1}} \mathbf{m}_{k-1} \\ &= {}^W \mathbf{L}_{k-1} {}^{L_{k-1}} \mathbf{H}_k {}^W \mathbf{L}_{k-1}^{-1} {}^W \mathbf{m}_{k-1} \\ &= {}_{k-1}^W \mathbf{H}_k {}^W \mathbf{m}_{k-1} \end{aligned} \quad (42)$$

where ${}_{k-1}^W \mathbf{H}_k := {}^W \mathbf{L}_{k-1} {}^{L_{k-1}} \mathbf{H}_k {}^W \mathbf{L}_{k-1}^{-1}$, an operation referred to as *a frame change of a pose transformation* by Chirikjian *et al.* [23].

B. Constant motion model in different frames

As discussed in [11], we can show that if the body-fixed frame pose change is constant then the absolute reference

frame change is constant too:

$$\begin{aligned} {}_{k-1}^W \mathbf{H}_k &= C = {}_k^L \mathbf{H}_{k+1} \\ {}_{k-1}^W \mathbf{H}_k &= {}^W \mathbf{L}_{k-1} C {}^W \mathbf{L}_{k-1}^{-1} \\ {}_k^W \mathbf{H}_{k+1} &= {}^W \mathbf{L}_k C {}^W \mathbf{L}_k^{-1} \end{aligned}$$

given that, ${}^W \mathbf{L}_k = {}^W \mathbf{L}_{k-1} C$ (43)

$$\begin{aligned} {}_k^W \mathbf{H}_{k+1} &= {}^W \mathbf{L}_{k-1} C C C^{-1} {}^W \mathbf{L}_{k-1}^{-1} \\ &= {}^W \mathbf{L}_{k-1} C {}^W \mathbf{L}_{k-1}^{-1} \\ &= {}_{k-1}^W \mathbf{H}_k \end{aligned}$$

This equations shows that when the change in local motion is constant, the corresponding change in absolute motion is also constant. However, when the change in local motion is not constant, the change in absolute motion actually scales with distance the object is from $\{W\}$. This relationship is highly relevant relevant for the object smoothing factor in Eq. (18) which enforces a constant motion constraint in the $\{W\}$ frame. Let the change in local motion be defined as:

$${}^L \mathbf{C} = {}_k^L \mathbf{H}_{k+1}^{-1} {}_{k+1}^{L_{k+1}} \mathbf{H}_{k+2} \in \text{SE}(3) \quad (44)$$

and the change in absolute motion:

$${}^W \mathbf{C} = {}_k^W \mathbf{H}_{k+1}^{-1} {}_{k+1}^W \mathbf{H}_{k+2} \in \text{SE}(3) \quad (45)$$

We can then say:

$$\begin{aligned} {}_k^W \mathbf{H}_{k+1} &= {}^W \mathbf{L}_{k+1} {}^W \mathbf{L}_k^{-1} \\ {}_{k+1}^W \mathbf{H}_{k+2} &= {}^W \mathbf{L}_{k+2} {}^W \mathbf{L}_{k+1}^{-1} \\ &= {}^W \mathbf{L}_{k+1} {}^W \mathbf{L}_k^{-1} {}^W \mathbf{L}_{k+1} {}^L \mathbf{C} {}^W \mathbf{L}_{k+1}^{-1} \\ &= {}_k^W \mathbf{H}_{k+1} {}^W \mathbf{L}_{k+1} {}^L \mathbf{C} {}^W \mathbf{L}_{k+1}^{-1} \end{aligned} \quad (46)$$

Substituting Eq. (46) into Eq. (45) defines the relationship between the change in motion when represented in the local-body and world frames:

$${}^W \mathbf{C} = {}^W \mathbf{L}_{k+1} {}^L \mathbf{C} {}^W \mathbf{L}_{k+1}^{-1} \quad (47)$$

Consequently, the residual and covariance of the object smoothing factor will increase proportionally with the object’s pose. To mitigate this effect for our smaller-scale experiments, we set the covariance of the smoothing factor to a sufficiently large value.

REFERENCES

- [1] D. M. Rosen, K. J. Doherty, A. Terán Espinoza, and J. J. Leonard, “Advances in inference and representation for simultaneous localization and mapping,” *Annual Review of Control, Robotics, and Autonomous Systems*, vol. 4, no. 1, pp. 215–242, 2021.
- [2] R. A. Newcombe, S. Izadi, O. Hilliges, D. Molyneaux, D. Kim, A. J. Davison, P. Kohi, J. Shotton, S. Hodges, and A. Fitzgibbon, “Kinectfusion: Real-time dense surface mapping and tracking,” in *IEEE/ACM Intl. Symp. on Mixed and Augmented Reality (ISMAR)*, 2011, pp. 127–136.
- [3] R. Mur-Artal and J. D. Tardós, “Orb-slam2: An open-source slam system for monocular, stereo, and rgbd cameras,” *IEEE Trans. Robotics*, vol. 33, no. 5, pp. 1255–1262, 2017.
- [4] C. Campos, R. Elvira, J. J. Gómez, J. M. M. Montiel, and J. D. Tardós, “ORB-SLAM3: An accurate open-source library for visual, visual-inertial and multi-map SLAM,” *IEEE Trans. Robotics*, vol. 37, no. 6, pp. 1874–1890, 2021.
- [5] H. Zhao, M. Chiba, R. Shibasaki, X. Shao, J. Cui, and H. Zha, “SLAM in a dynamic large outdoor environment using a laser scanner,” in *Proc. of the IEEE Intl. Conf. on Robotics and Automation (ICRA)*, 2008, pp. 1455–1462.

[6] B. Bescos, J. M. Fácil, J. Civera, and J. Neira, "Dynaslam: Tracking, mapping, and inpainting in dynamic scenes," *IEEE Robotics and Automation Letters*, vol. 3, no. 4, pp. 4076–4083, 2018.

[7] R. A. Newcombe, D. Fox, and S. M. Seitz, "Dynamicfusion: Reconstruction and tracking of non-rigid scenes in real-time," in *Proc. of the IEEE Intl. Conf. Computer Vision and Pattern Recognition*, June 2015.

[8] Y. Wang, J. Morris, L. Wu, T. Vidal-Calleja, and V. Ila, "Dynorecon: Dynamic object reconstruction for navigation," *arXiv preprint arXiv:2409.19928*, 2024.

[9] M. N. Finean, W. Merkt, and I. Havoutis, "Simultaneous scene reconstruction and whole-body motion planning for safe operation in dynamic environments," in *Proc. of the IEEE/RSJ Intl. Conf. on Intelligent Robots and Systems (IROS)*, 2021, pp. 3710–3717.

[10] A. Hermann, J. Bauer, S. Klemm, and R. Dillmann, "Mobile manipulation planning optimized for gpgpu voxel-collision detection in high resolution live 3d-maps," in *Intl. Symp. on Robotics/Robotik*, 2014, pp. 1–8.

[11] M. Henein, J. Zhang, R. Mahony, and V. Ila, "Dynamic SLAM: The Need for Speed," in *Proc. of the IEEE Intl. Conf. on Robotics and Automation (ICRA)*, 2020, pp. 2123–2129.

[12] C.-C. Wang, C. Thorpe, S. Thrun, M. Hebert, and H. Durrant-Whyte, "Simultaneous localization, mapping and moving object tracking," *Intl. J. of Robotics Research*, vol. 26, no. 9, pp. 889–916, 2007.

[13] A. Deep, Y.-J. Pan, and M. L. Seto, "Model-based quasi-static slam in unstructured dynamic environments," in *IEEE International Conference on Automation Science and Engineering (CASE)*, 2021, pp. 196–201.

[14] T. P. Setterfield, D. W. Miller, J. J. Leonard, and A. Saenz-Otero, "Mapping and determining the center of mass of a rotating object using a moving observer," *Intl. J. of Robotics Research*, vol. 37, no. 1, pp. 83–103, 2018.

[15] J. Zhang, M. Henein, R. Mahony, and V. Ila, "VDO-SLAM: A Visual Dynamic Object-aware SLAM System," *arXiv preprint arXiv:2005.11052*, 2020.

[16] Y. Liu, C. Guo, Y. Luo, and Y. Wang, "Dynameshslam: A mesh-based dynamic visual slammot method," *IEEE Robotics and Automation Letters*, vol. 9, no. 6, pp. 5791–5798, 2024.

[17] K. M. Judd and J. D. Gammell, "Multimotion Visual Odometry (MVO)," *Intl. J. of Robotics Research*, 2024.

[18] J. Morris, Y. Wang, and V. Ila, "The importance of coordinate frames in dynamic slam," in *Proc. of the IEEE Intl. Conf. on Robotics and Automation (ICRA)*, 2024.

[19] R. Tian, Y. Zhang, L. Yang, J. Zhang, S. Coleman, and D. Kerr, "Dynaquadric: Dynamic quadric slam for quadric initialization, mapping, and tracking," *IEEE Trans. on Intelligent Transportation Systems*, vol. 25, no. 11, pp. 17234–17246, 2024.

[20] K. M. Judd, J. D. Gammell, and P. Newman, "Multimotion visual odometry (MVO): Simultaneous estimation of camera and third-party motions," in *Proc. of the IEEE/RSJ Intl. Conf. on Intelligent Robots and Systems (IROS)*. IEEE, 2018, pp. 3949–3956.

[21] B. Bescos, C. Campos, J. D. Tardós, and J. Neira, "Dynaslam ii: Tightly-coupled multi-object tracking and slam," *IEEE Robotics and Automation Letters*, vol. 6, no. 3, pp. 5191–5198, 2021.

[22] K. M. Judd and J. D. Gammell, "The Oxford Multimotion Dataset: Multiple SE(3) Motions with Ground Truth," *IEEE Robotics and Automation Letters*, vol. 4, no. 2, pp. 800–807, 2019.

[23] G. S. Chirikjian, R. Mahony, S. Ruan, and J. Trumpf, "Pose changes from a different point of view," in *Proc. of the ASME Intl. Design Engineering Technical Conf. (IDETC)*. ASME, 2017.

[24] J. Huang, S. Yang, Z. Zhao, Y. Lai, and S. Hu, "Clusterslam: A slam backend for simultaneous rigid body clustering and motion estimation," in *Proc. of the Intl. Conf. on Computer Vision (ICCV)*, 2019, pp. 5874–5883.

[25] D. Thomas, W. Woodall, and E. Fernandez, "Next-generation ROS: Building on DDS," in *ROSCon Chicago 2014*. Mountain View, CA: Open Robotics, sep 2014.

[26] A. Rosinol, M. Abate, Y. Chang, and L. Carlone, "Kimera: an open-source library for real-time metric-semantic localization and mapping," in *Proc. of the IEEE Intl. Conf. on Robotics and Automation (ICRA)*, 2020.

[27] S. Song, H. Lim, A. J. Lee, and H. Myung, "Dynavins: A visual-inertial slam for dynamic environments," *IEEE Robotics and Automation Letters*, vol. 7, no. 4, pp. 11523–11530, 2022.

[28] M. A. Fischler and R. C. Bolles, "Random sample consensus: a paradigm for model fitting with applications to image analysis and automated cartography," *Communications of the ACM*, vol. 24, no. 6, pp. 381–395, 1981.

[29] W. Dai, Y. Zhang, P. Li, Z. Fang, and S. Scherer, "Rgb-d slam in dynamic environments using point correlations," *IEEE Trans. Pattern Analysis and Machine Intelligence*, vol. 44, no. 1, pp. 373–389, 2022.

[30] S. Song, H. Lim, A. J. Lee, and H. Myung, "Dynavins++: Robust visual-inertial state estimator in dynamic environments by adaptive truncated least squares and stable state recovery," *IEEE Robotics and Automation Letters*, 2024.

[31] R. Hachiuma, C. Pirchheim, D. Schmalstieg, and H. Saito, "Detect-fusion: Detecting and segmenting both known and unknown dynamic objects in real-time slam," *arXiv preprint arXiv:1907.09127*, 2019.

[32] T. Zhang, H. Zhang, Y. Li, Y. Nakamura, and L. Zhang, "Flowfusion: Dynamic dense rgb-d slam based on optical flow," in *Proc. of the IEEE Intl. Conf. on Robotics and Automation (ICRA)*. IEEE, 2020, pp. 7322–7328.

[33] L. Schmid, M. Abate, Y. Chang, and L. Carlone, "Khronus: A unified approach for spatio-temporal metric-semantic slam in dynamic environments," in *Proc. of the Robotics: Science and Systems (RSS)*, 2024.

[34] L. Schmid, O. Andersson, A. Sulser, P. Pfreundschuh, and R. Siegwart, "Dynablox: Real-time detection of diverse dynamic objects in complex environments," *IEEE Robotics and Automation Letters*, vol. 8, no. 10, pp. 6259 – 6266, 2023.

[35] J. Huang, S. Yang, T.-J. Mu, and S.-M. Hu, "Clustervo: Clustering moving instances and estimating visual odometry for self and surroundings," in *Proc. of the IEEE/CVF Intl. Conf. Computer Vision and Pattern Recognition*, 2020, pp. 2168–2177.

[36] I. A. Bârsan, P. Liu, M. Pollefeys, and A. Geiger, "Robust Dense Mapping for Large-Scale Dynamic Environments," in *Proc. of the IEEE Intl. Conf. on Robotics and Automation (ICRA)*, 2018.

[37] C.-C. Wang, C. Thorpe, S. Thrun, M. Hebert, and H. Durrant-Whyte, "Simultaneous localization, mapping and moving object tracking," *Intl. J. of Robotics Research*, vol. 26, no. 9, pp. 889–916, 2007.

[38] I. Ballester, A. Fontán, J. Civera, K. H. Strobl, and R. Triebel, "Dot: Dynamic object tracking for visual slam," in *Proc. of the IEEE Intl. Conf. on Robotics and Automation (ICRA)*, 2021, pp. 11705–11711.

[39] S. Yang and S. Scherer, "Cubeslam: Monocular 3-d object slam," *IEEE Trans. Robotics*, vol. 35, no. 4, pp. 925–938, 2019.

[40] P. Li, T. Qin, et al., "Stereo vision-based semantic 3d object and ego-motion tracking for autonomous driving," in *Proc. of the European Conf. on Computer Vision (ECCV)*, 2018, pp. 646–661.

[41] M. Gonzalez, E. Marchand, A. Kacete, and J. Royan, "Twistslam: Constrained slam in dynamic environment," *IEEE Robotics and Automation Letters*, vol. 7, no. 3, pp. 6846–6853, 2022.

[42] M. Gonzalez, E. Marchand, A. Kacete, and J. Royan, "Twistslam++: Fusing multiple modalities for accurate dynamic semantic slam," in *Proc. of the IEEE/RSJ Intl. Conf. on Intelligent Robots and Systems (IROS)*. IEEE, 2023, pp. 9126–9132.

[43] L. Nicholson, M. Milford, and N. Sündnerhauf, "QuadricsLAM: Dual Quadrics as SLAM Landmarks," in *Proc. of the IEEE/CVF Intl. Conf. Computer Vision and Pattern Recognition*, 2018, pp. 313–314.

[44] Q. Zhang, Y. Yang, H. Fang, R. Geng, and P. Jensfelt, "Deflow: Decoder of scene flow network in autonomous driving," *arXiv preprint arXiv:2401.16122*, 2024.

[45] Q. Zhang, Y. Yang, P. Li, O. Andersson, and P. Jensfelt, "Seflow: A self-supervised scene flow method in autonomous driving," *arXiv preprint arXiv:2407.01702*, 2024.

[46] Z. Wang, Y. Wei, Y. Rao, J. Zhou, and J. Lu, "3d point-voxel correlation fields for scene flow estimation," *IEEE Trans. Pattern Analysis and Machine Intelligence*, vol. 45, no. 11, pp. 13 621–13 635, 2023.

[47] X. Li, J. Zheng, F. Ferroni, J. K. Pontes, and S. Lucey, "Fast neural scene flow," in *Proc. of the Intl. Conf. on Computer Vision (ICCV)*, 2023, pp. 9844–9856.

[48] D. F. Henning, C. Choi, S. Schaefer, and S. Leutenegger, "Bodyslam++: Fast and tightly-coupled visual-inertial camera and human motion tracking," in *Proc. of the IEEE/RSJ Intl. Conf. on Intelligent Robots and Systems (IROS)*, 2023, pp. 3781–3788.

[49] J. Wang, M. Rünz, and L. Agapito, "Dsp-slam: Object oriented slam with deep shape priors," in *Proc. of Intl. Conf. on 3D Vision*, 2021, pp. 1362–1371.

[50] Y. Qiu, C. Wang, W. Wang, M. Henein, and S. Scherer, "Airdos: Dynamic slam benefits from articulated objects," in *Proc. of the IEEE Intl. Conf. on Robotics and Automation (ICRA)*, 2022, pp. 8047–8053.

[51] J. Zhang, M. Henein, R. Mahony, and V. Ila, "Robust Ego and Object 6-DoF Motion Estimation and Tracking," in *Proc. of the IEEE/RSJ Intl. Conf. on Intelligent Robots and Systems (IROS)*, 2020, pp. 5017–5023.

[52] H.-S. Fang, S. Xie, Y.-W. Tai, and C. Lu, "Rmpe: Regional multi-person pose estimation," in *Proc. of the Intl. Conf. on Computer Vision (ICCV)*, 2017, pp. 2353–2362.

[53] P. J. Huber, “Robust estimation of a location parameter,” in *Breakthroughs in statistics*. Springer, 1992, pp. 492–518.

[54] F. Dellaert and GTSAM Contributors, “borglab/gtsam,” May 2022. [Online]. Available: <https://github.com/borglab/gtsam>

[55] G. Farnebäck, “Two-frame motion estimation based on polynomial expansion,” in *Image Analysis: 13th Scandinavian Conference, SCIA 2003 Halmstad, Sweden, June 29–July 2, 2003 Proceedings 13*. Springer, 2003, pp. 363–370.

[56] Z. Teed and J. Deng, “Raft: Recurrent all-pairs field transforms for optical flow,” in *Proc. of the European Conf. on Computer Vision (ECCV)*. Springer, 2020, pp. 402–419.

[57] J. Shi *et al.*, “Good features to track,” in *1994 Proceedings of IEEE conference on computer vision and pattern recognition*. IEEE, 1994, pp. 593–600.

[58] E. Rublee, V. Rabaud, K. Konolige, and G. Bradski, “Orb: An efficient alternative to sift or surf,” in *2011 International Conference on Computer Vision*, 2011, pp. 2564–2571.

[59] B. D. Lucas and T. Kanade, “An iterative image registration technique with an application to stereo vision,” in *IJCAI’81: 7th international joint conference on Artificial intelligence*, vol. 2, 1981, pp. 674–679.

[60] O. Bailo, F. Rameau, K. Joo, J. Park, O. Bogdan, and I. S. Kweon, “Efficient adaptive non-maximal suppression algorithms for homogeneous spatial keypoint distribution,” *Pattern Recognition Letters*, vol. 106, pp. 53–60, 2018.

[61] Y. Zhang, P. Sun, Y. Jiang, D. Yu, F. Weng, Z. Yuan, P. Luo, W. Liu, and X. Wang, “Bytetrack: Multi-object tracking by associating every detection box,” in *Proc. of the European Conf. on Computer Vision (ECCV)*. Springer, 2022, pp. 1–21.

[62] T. Ke and S. I. Roumeliotis, “An efficient algebraic solution to the perspective-three-point problem,” in *Proc. of the IEEE Intl. Conf. Computer Vision and Pattern Recognition*, 2017.

[63] L. Kneip and P. Furgale, “Opengv: A unified and generalized approach to real-time calibrated geometric vision,” in *Proc. of the IEEE Intl. Conf. on Robotics and Automation (ICRA)*. IEEE, 2014, pp. 1–8.

[64] M. Grupp, “evo: Python package for the evaluation of odometry and slam.” <https://github.com/MichaelGrupp/evo>, 2017.

[65] J. Sturm, N. Engelhard, F. Endres, W. Burgard, and D. Cremers, “A benchmark for the evaluation of rgb-d slam systems,” in *Proc. of the IEEE/RSJ Intl. Conf. on Intelligent Robots and Systems (IROS)*. IEEE, 2012, pp. 573–580.

[66] A. Geiger, P. Lenz, C. Stiller, and R. Urtasun, “Vision meets robotics: The KITTI dataset,” *Intl. J. of Robotics Research*, vol. 32, no. 11, pp. 1231–1237, 2013.

[67] S. Umeyama, “Least-squares estimation of transformation parameters between two point patterns,” *IEEE Trans. Pattern Analysis and Machine Intelligence*, vol. 13, no. 04, pp. 376–380, 1991.

[68] A. Dosovitskiy, G. Ros, F. Codevilla, A. Lopez, and V. Koltun, “CARLA: An open urban driving simulator,” in *Proc. of the Conf. on Robot Learning (CoRL)*, 2017, pp. 1–16.

[69] L. Carlone, Z. Kira, C. Beall, V. Indelman, and F. Dellaert, “Eliminating conditionally independent sets in factor graphs: A unifying perspective based on smart factors,” in *Proc. of the IEEE Intl. Conf. on Robotics and Automation (ICRA)*. IEEE, 2014, pp. 4290–4297.

[70] M. Nießner, M. Zollhöfer, S. Izadi, and M. Stamminger, “Real-time 3d reconstruction at scale using voxel hashing,” *ACM Transactions on Graphics (TOG)*, 2013.

[71] O. Kahler, V. A. Prisacariu, C. Y. Ren, X. Sun, P. H. S. Torr, and D. W. Murray, “Very High Frame Rate Volumetric Integration of Depth Images on Mobile Device,” *IEEE Trans. on Visualization and Computer Graphics*, vol. 22, no. 11, 2015.

[72] M. Phillips and M. Likhachev, “Sipp: Safe interval path planning for dynamic environments,” in *Proc. of the IEEE Intl. Conf. on Robotics and Automation (ICRA)*, 2011, pp. 5628–5635.

[73] M. N. Finean, W. Merkt, and I. Havoutis, “Predicted composite signed-distance fields for real-time motion planning in dynamic environments,” in *Proc. of the Conf. on Automated Planning and Scheduling*, vol. 31, 2021, pp. 616–624.

[74] M. N. Finean, L. Petrović, W. Merkt, I. Marković, and I. Havoutis, “Motion planning in dynamic environments using context-aware human trajectory prediction,” *J. of Robotics and Autonomous Systems*, vol. 166, p. 104450, 2023.

[75] T. Salzmann, B. Ivanovic, P. Chakravarty, and M. Pavone, “Trajectron++: Dynamically-feasible trajectory forecasting with heterogeneous data,” in *Proc. of the European Conf. on Computer Vision (ECCV)*. Springer, 2020, pp. 683–700.

[76] B. Ivanovic, J. Harrison, and M. Pavone, “Expanding the deployment envelope of behavior prediction via adaptive meta-learning,” in *Proc. of the IEEE Intl. Conf. on Robotics and Automation (ICRA)*, 2023.

[77] M. King-Smith, P. Tsotras, and F. Dellaert, “Simultaneous control and trajectory estimation for collision avoidance of autonomous robotic spacecraft systems,” in *Proc. of the IEEE Intl. Conf. on Robotics and Automation (ICRA)*. IEEE, 2022, pp. 257–264.

[78] N. Ravi, V. Gabeur, Y.-T. Hu, R. Hu, C. Ryali, T. Ma, H. Khedr, R. Rädel, C. Rolland, L. Gustafson, *et al.*, “Sam 2: Segment anything in images and videos,” *arXiv preprint arXiv:2408.00714*, 2024.

[79] C.-Y. Yang, H.-W. Huang, W. Chai, Z. Jiang, and J.-N. Hwang, “Samurai: Adapting segment anything model for zero-shot visual tracking with motion-aware memory,” 2024.

[80] Z. Huang, X. Shi, C. Zhang, Q. Wang, K. C. Cheung, H. Qin, J. Dai, and H. Li, “Flowformer: A transformer architecture for optical flow,” in *Proc. of the European Conf. on Computer Vision (ECCV)*. Springer, 2022, pp. 668–685.



Jesse Morris is a 3rd year PhD student at the Australian Centre For Robotics, supervised by Dr Viorela Ila. His thesis focuses on developing estimation frameworks for Dynamic SLAM. He received his bachelors degree in Mechatronic Engineering and Computer Science from the University of Sydney in 2022.



Yiduo Wang has been a postdoctoral researcher in the Australian Centre For Robotics since December 2022, working with Dr Viorela Ila. He focuses on SLAM, reconstruction and navigation in dynamic environments. He holds a DPhil Engineering Science degree awarded by University of Oxford, where his research focused on large-scale reconstruction. He also holds an MRes Robotics degree awarded by UCL on combining SLAM with semantic segmentation for dynamic environments. His research interests lies in SLAM and autonomous exploration.



Mikolaj Kliniewski is a 2nd year PhD student at the Australian Centre For Robotics, supervised by Dr Viorela Ila. His thesis focuses on joint planning and estimation in dynamic environments. He received his Bachelor Honours degree in Computer Science from the University of Liverpool in 2023.



Viorela Ila received a Ph.D. in Information Technologies from the Universitat de Girona, Spain. She worked at the Institut de Robòtica i Informàtica Industrial, Barcelona, and was awarded a MICINN/FULBRIGHT post-doctoral fellowship in 2009, joining Georgia Tech, USA. She joined the ROSACE project in LAAS-CNRS, France, in 2010, and was a Research Scientist at Brno University of Technology, Czech Republic (2012–2014) and a Research Fellow at the Australian National University (2015–2018). Currently a Senior Lecturer at the University of Sydney, her research focuses on robot vision, SLAM and 3D reconstruction, leveraging graphical models, optimization methods and information theory.